Journal of Petroleum Science and Engineering 219 (2022) 111109

Contents lists available at ScienceDirect

Journal of Petroleum Science and Engineering

journal homepage: www.elsevier.com/locate/petrol

Joint inversion of the unified pore geometry of tight sandstones based on elastic and electrical properties

Lin Zhang [a,b], Jing Ba [a,*], Chao Li [a], José M. Carcione [c], Feng Zhou [d]

[a] School of Earth Sciences and Engineering, Hohai University, Nanjing, China
[b] Earth Atmospheric, and Planetary Sciences Department, Purdue University, West Lafayette, IN, USA
[c] National Institute of Oceanography and Applied Geophysics – OGS, Trieste, Italy
[d] SINOPEC Geophysical Research Institute, Nanjing, China

ARTICLE INFO

Keywords:
Tight sandstone
Pore geometry
Ultrasonic wave velocities
Electrical conductivity
Porosity
Static elastic moduli

ABSTRACT

The prediction of the pore geometrical properties is important in the exploration and development of tight-sandstone hydrocarbon reservoirs. To investigate this topic, we have measured the porosity, permeability, P- and S-wave velocities, electrical conductivity, and axial and radial strains as a function of differential (confining minus pore) pressure of tight-sandstone samples, collected from the Zhongjiang gas field of Sichuan, in West China. The results show that the closure of cracks with pressure highly affects these properties. Then, we propose a multiphase reformulated differential effective-medium (R-DEM) model that employs the unified pore geometry (the same pores or cracks with different aspect ratios and volume fractions) for both elastic and electrical modeling. The model gives the pressure-dependence of the P- and S-wave velocities and electrical conductivity, and the experimental porosity and static moduli are used as constraints to estimate the pore geometry. The model describes the elastic properties of sandstones saturated with nitrogen gas, and the electrical conductivity when the pore fluid is brine. The prediction of the wet-rock S-wave velocities is less accurate, due to the presence of shear stiffening and weakening effects. Furthermore, we compare the results with those of the joint elastic-electrical inversion by using the dynamic instead of the static stiffness modulus. The results show that the latter provides a better agreement between theory and experiment. Subsequently, we show that the pore geometry estimated from the elastic or the electrical measurements separately (unjoint inversion) present discrepancies, indicating that a joint inversion is required. The published experimental data are also used to illustrate the model, and the results are satisfactory.

1. Introduction

Tight-sandstone hydrocarbon reservoirs, an important and potential unconventional resource, have generally low porosity and permeability, and complex pore geometries (Lai et al., 2018). The pore geometry, and the size, spatial distribution and connectivity of pores and cracks play a major role on the physical (elastic-electrical) properties (e.g., Carcione, 2022; Cheng et al., 2020a, b; Sheng, 1991; Tran et al., 2008; Wang et al., 2021; Zhang et al., 2019a). Hence, to reduce the uncertainties in the reservoir characterization, it is essential to estimate the pore geometry from those properties.

Effective-medium models have been proposed to relate the pore geometry and elastic properties (Benveniste, 1987; Berryman, 1995; Carcione et al., 2003; Eshelby, 1957; Fortin et al., 2007; Kachanov, 1993; Kuster and Toksöz, 1974; Le Ravalec and Guéguen, 1996; Mori and Tanaka, 1973; Walsh, 1965; Wu, 1966), electrical properties (Bruggeman, 1935; Berg, 2007; Carcione et al., 2003; Garnett, 1904, 1906; Gelius and Wang, 2008; Han et al., 2015; Seleznev et al., 2006), transport properties (Al-Wardy and Zimmerman, 2004; Guéguen and Schubnel, 2003; Sarout, 2012), and thermal properties (e.g., Pimienta et al., 2014a). The pore geometry can be estimated from these properties by considering the closure or dilation of pores and cracks with different aspect ratios as a function of pressure (Cheng, 1978; Cheng and Toksöz, 1979; David and Zimmerman, 2012; Izumotani and Onozuka, 2013; Tang et al., 2021; Wang and Tang, 2021). However, most of these models consider a single property, while a better estimation can be obtained with multiple properties (e.g., Gomez et al., 2010; Han, 2018; Pimienta et al., 2017; Sarout et al., 2017; Watanabe and Higuchi, 2015;

* Corresponding author.
E-mail address: jingba@188.com (J. Ba).

https://doi.org/10.1016/j.petrol.2022.111109
Received 25 July 2022; Received in revised form 19 September 2022; Accepted 30 September 2022
Available online 6 October 2022
0920-4105/© 2022 Elsevier B.V. All rights reserved.

Table 1
Physical properties of the samples.

Sample	TS1	TS2	TS3
Porosity (%)	10.10	6.79	11.96
Dry density (kg/m^3)	2390	2470	2340
Permeability (mD)	0.2203	0.1705	0.7294
Quartz (%)	24.6	14.6	47.9
Potassium feldspar (%)	0.4	–	1.0
Plagioclase (%)	59.1	72.8	36.4
Clay (%)	13.4	11.7	14.1
Calcite (%)	0.4	0.4	0.4
Dolomite (%)	1.0	–	–
Siderite (%)	0.1	0.2	0.1
Pyrite (%)	1.0	0.3	0.1

Watanabe et al., 2019; Yan et al., 2014; Zhang et al., 2020). Different models yield dissimilar results and the reason is due to the different orders in which the rock components are added in the modeling process. In the self-consistent (SC) model all the components are treated equally with no preferential host medium (e.g., Berryman, 1992, 1995; Berge et al., 1993; Norris et al., 1985). This model has been widely used for a joint evaluation of the elastic (P and S velocities) and electrical properties (Aquino-López et al., 2011, 2015; Kazatchenko et al., 2004, 2006). Using the SC model, Han et al. (2016) estimated the pore geometry of a sandstone from the elastic velocities and electrical conductivities measured as a function of the differential pressure P_d, but their results show a misfit between measurements and predictions. This misfit may be due to an overestimation of the effect of pores or cracks on the elastic moduli (Bruner, 1976).

On the other hand, the differential effective-medium (DEM) model is also adopted to model the physical properties, where the fluid-filled pores are inclusions added into a background/host or frame (matrix) (elastic modeling), and the solid particles are inclusions embedded into a fluid background (electrical modeling) (e.g., Berryman, 1995; Cosenza et al., 2003; Gelius and Wang, 2008; Markov et al., 2005). These different approaches can be inconsistent to estimate the pore geometry. Han et al. (2020) obtained the pore and grain aspect ratios from experimental P and S velocities and electrical conductivity of a clean sandstone, by using the elastic and electrical DEM models for a

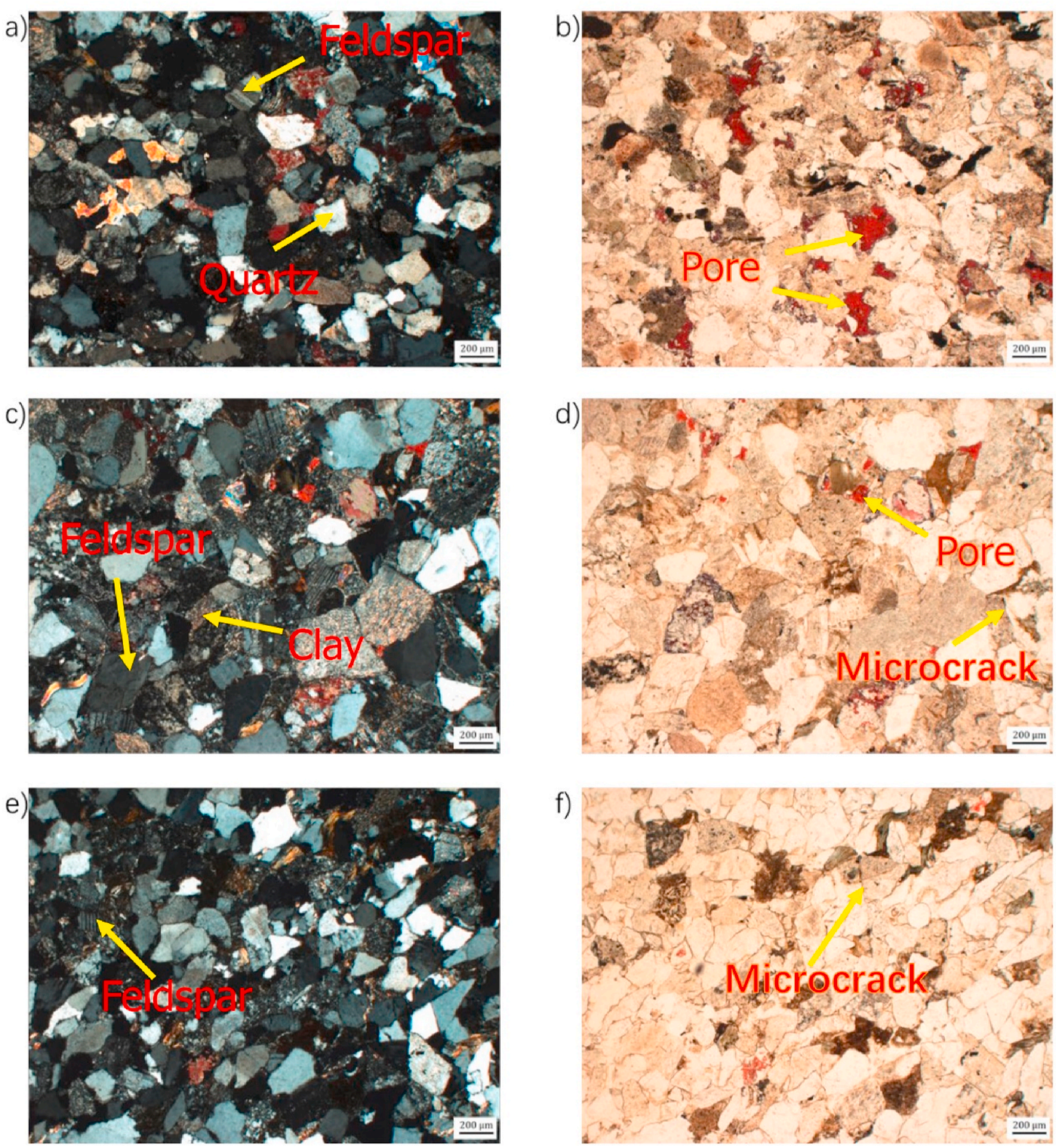

Fig. 1. Thin section of the tight-sandstone samples, under orthogonal (left) and single (right) polarization images. (a), (b) TS1 sample. (c), (d) TS2 sample. (e), (f) TS3 sample. The red color indicates the pore space. (For interpretation of the references to color in this figure legend, the reader is referred to the Web version of this article.)

Table 2
Physical properties of the pore fluids.

Fluid type	Density (kg/m^3)	Bulk modulus (GPa)	Electrical conductivity (S/m)
Nitrogen gas	112.6	0.0161	–
Water	1000	2.25	–
Brine	1000	2.25	8.2

two-phase medium. This study can be considered a continuation of the work of Cilli and Chapman (2018). Combining the SC and multiphase DEM models with the dual-porosity concept, Amalokwu and Falcon-Suarez (2021) modeled the joint properties of brine-saturated sandstones, based on the same pore geometry. To derive a cross-property DEM model from first principles, Cilli and Chapman (2021) reformulated the electrical DEM model for a two-phase medium (abbreviated 'R-DEM' henceforth), where fluid-filled pores are added as in the elastic modeling, and provided inspirations for obtaining a realistic estimation of the pore geometry.

In this study, we have performed experiments to analyze the pore geometry of tight sandstones. Basically, we have measured porosity, permeability, elastic velocities, electrical conductivity, and axial and radial strains as a function of the differential pressure. Then, the R-DEM model is extended to model the effects of multiple pores and cracks (multiphase R-DEM mode) on elastic and electrical properties, and a unified pore geometry is estimated from both properties by using the static moduli. The inversion result is used as an input to predict the elastic velocities of water-saturated rocks according to DEM model, and these predictions are compared with the experimental data. Then, we perform the same estimation using both the elastic and electrical properties by using the dynamic moduli, another estimation based on the elastic or the electrical properties by using the static moduli. Finally, we test the model with data of a clean sandstone.

2. Experiments

2.1. The samples

Three tight-sandstone samples (TS1, TS2 and TS3) were collected from the Jurassic Shaximiao Formation in the Sichuan Basin, West China. The samples are cylindrical of 49.68/49.06/45.65 mm length and 25.28/25.27/25.27 mm diameter. The ends of the samples were ground flat with a tolerance of ± 0.05 mm. The porosity (φ) and dry-rock density (ρ_{dry}) were obtained with a helium porosimeter, and the permeabilities

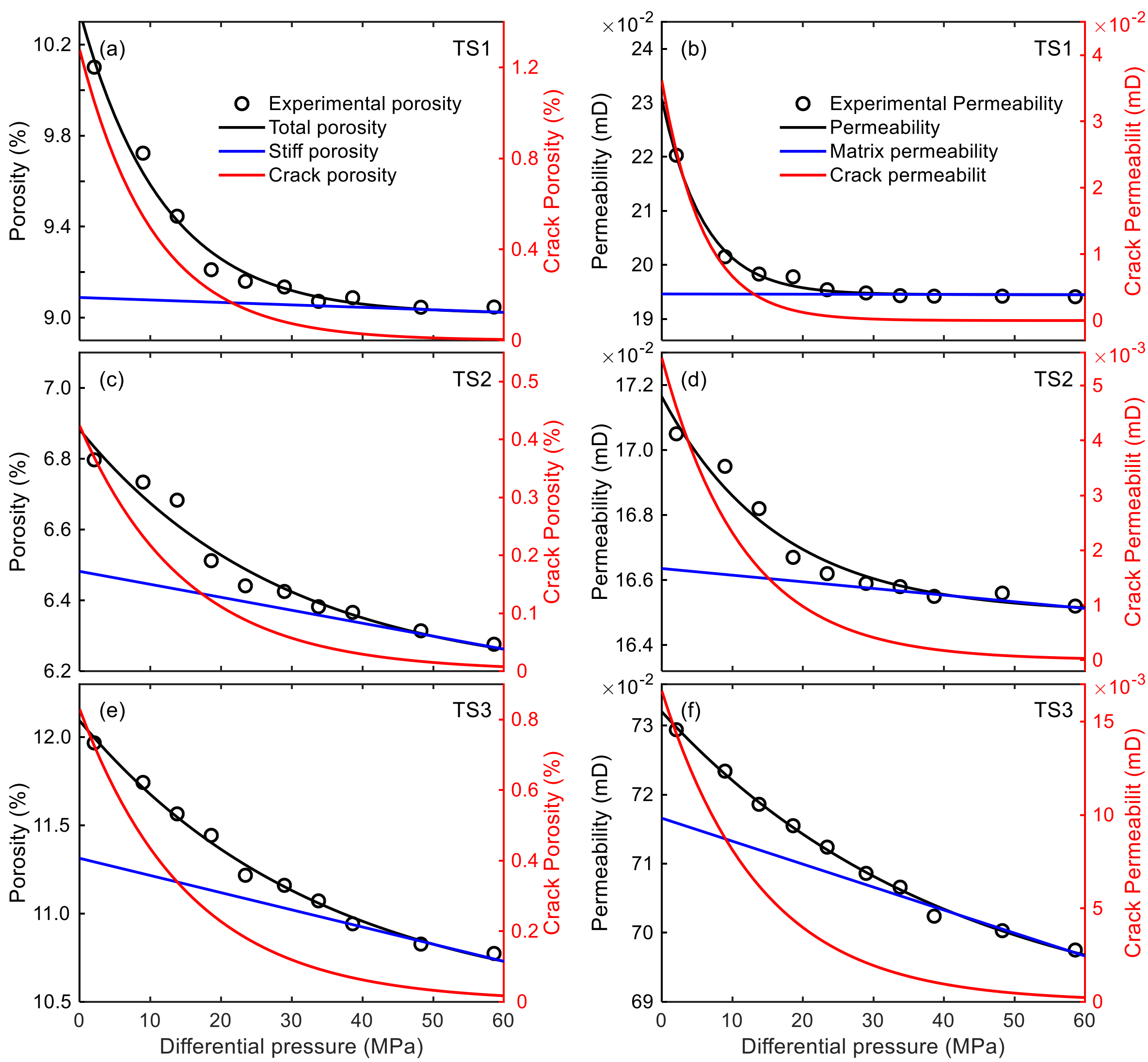

Fig. 2. Total, stiff and crack porosities and permeabilities as a function of differential pressure for samples TS1 (a, b), TS2 (c, d) and TS3 (e, f). The black circles denote the measurements, and the black, blue and red lines denote the fit curves of the total, stiff/matrix and crack porosities (permeabilities), respectively, according to the dual-porosity concept. (For interpretation of the references to color in this figure legend, the reader is referred to the Web version of this article.)

Table 3
Fit parameters for the pressure dependence of porosity and permeability.

Sample	TS1	TS2	TS3
Stiff porosity φ_s (%)	$9.1-0.0011P_d$	$6.5-0.00366P_d$	$11.31-0.01P_d$
Crack porosity φ_c(%)	$1.28e^{-0.095P_d}$	$0.42e^{-0.067P_d}$	$0.83e^{-0.065P_d}$
Matrix permeability κ_s (mD)	$0.195-0.000002P_d$	$0.167-0.00002P_d$	$0.717-0.00033P_d$
Crack permeability κ_c (mD)	$0.036e^{-0.169P_d}$	$0.0055e^{-0.086P_d}$	$0.017e^{-0.072P_d}$

Note that φ_s (κ_s) can be obtained by fitting the total porosities (permeabilities) at high differential pressures (with all the cracks closed). $\varphi_c(\kappa_c)$ is estimated by subtracting the stiff porosity (matrix permeability) from the total porosity (permeability).

measured with a helium porosimeter–permeameter based on the pulse-decay method. The details of the physical properties are listed in Table 1.

Fig. 1 shows thin sections of the samples, where we can see that the grains are compactly arranged with pore-contact cementation. The minerals are mainly quartz, feldspar and rock debris, and interstitial fillings consist of clays and calcite. The solid composition is estimated by X-ray diffraction analysis (see Table 1). In addition, the sections show that the intergranular pores are prominent in the TS1 sample (Fig. 1a and b), while the cracks within quartz grains (intragranular crack) are pervasive in the TS3 sample (Fig. 1e and f), which causes that the permeability of TS3 is higher than that of the other two.

2.2. Measurement procedure

We have performed the measurements as a function of differential pressure at room temperature. The properties of the pore fluids used in the tests are given in Table 2. More details of the experimental workflow are:

(1) The samples were washed several times to remove residual oil and salt, and placed in an oven at 70 °C for 48 h for drying. Then, they were slowly cooled to room temperature (25 °C) for several days.
(2) Helium porosity and permeability were measured at confining pressures (P_c) of 2.0685–58.6075 MPa and a constant pore pressure (P_p) of 1.379 MPa. Porosity is determined by using the helium expansion method, and permeability by using the unsteady-state pulse transient decay technique, corrected by the Klinkenberg slippage effect. The accuracy of the porosity and permeability measurements were ±0.5% and ±0.001mD, respectively.
(3) For the ultrasonic experiments with nitrogen gas as pore fluid, the confining pressure was first raised to 12 MPa, and then the pore

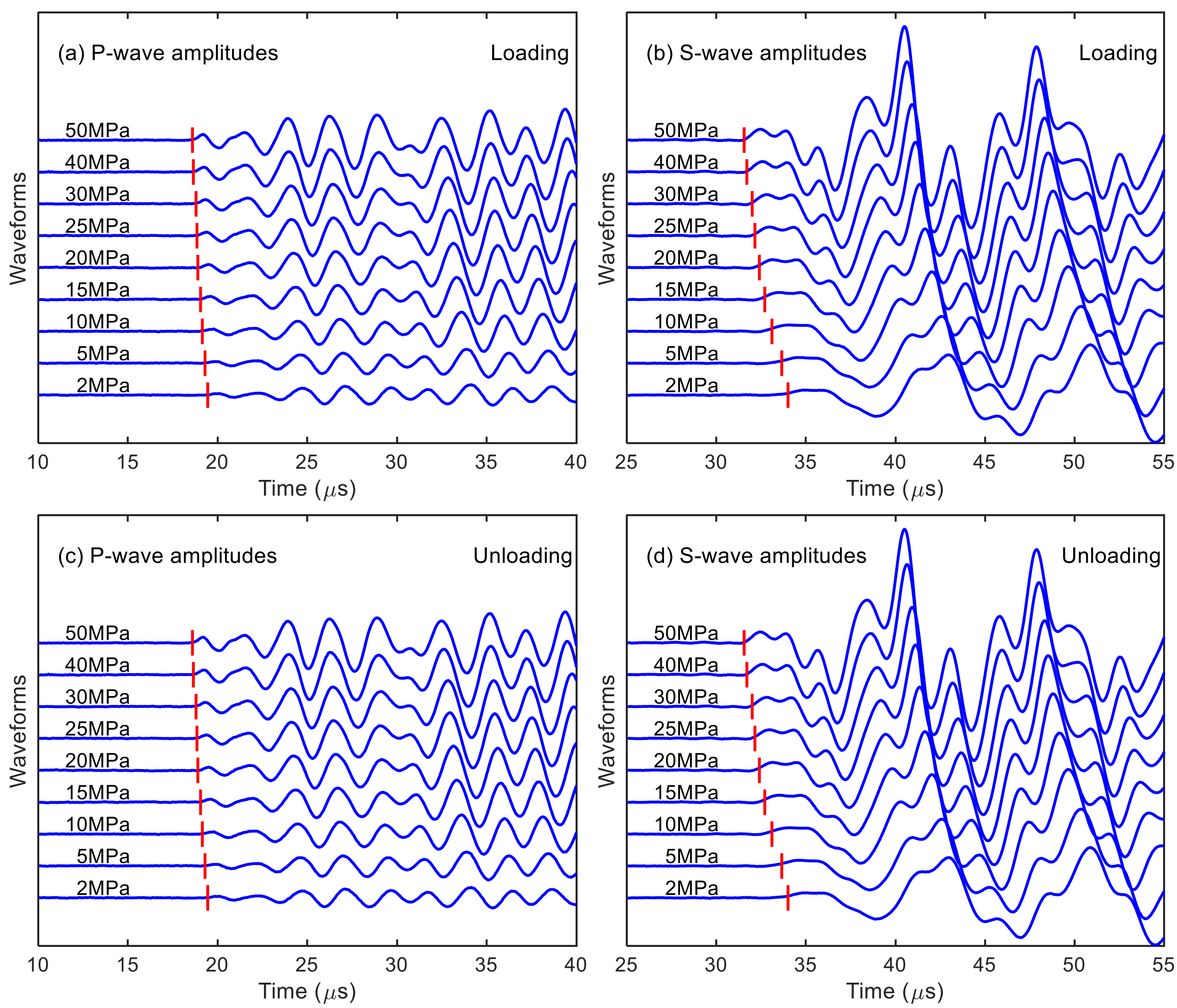

Fig. 3. Measured ultrasonic waveforms of water-saturated TS3 sample at different differential pressures. (a) and (c) P-wave signals received at loading and unloading processes; (b) and (d) S-wave signals received at loading and unloading processes. The red vertical bars represent the first arrival position. (For interpretation of the references to color in this figure legend, the reader is referred to the Web version of this article.)

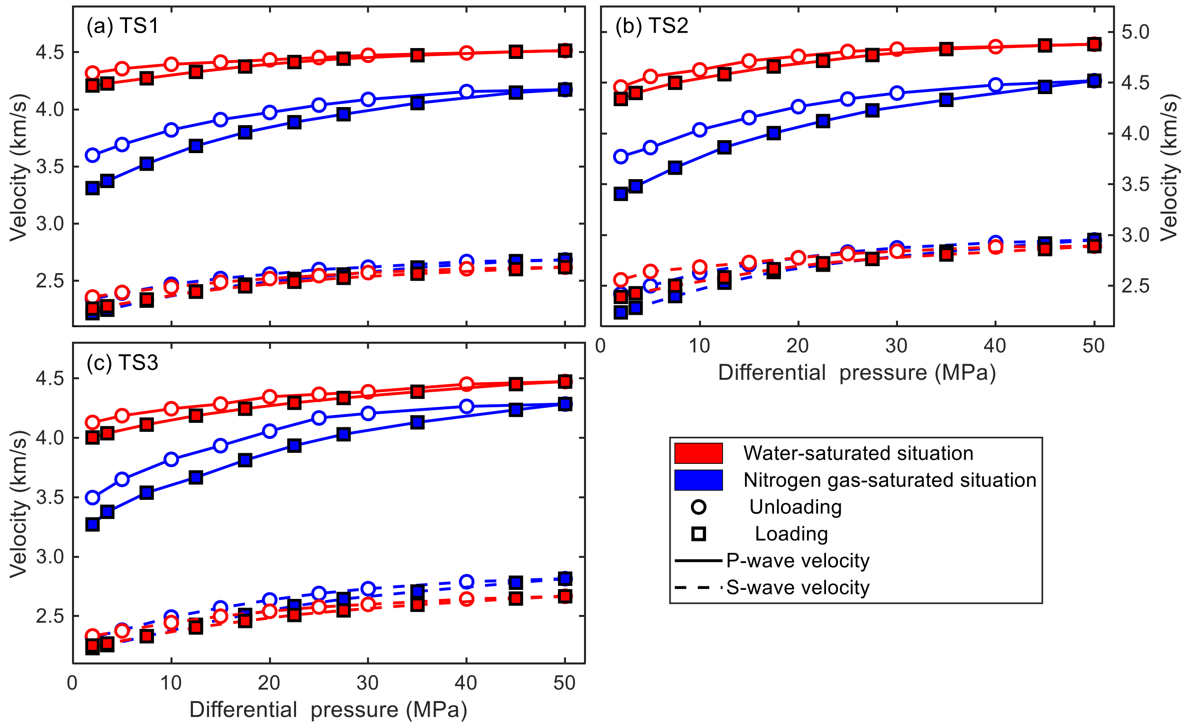

Fig. 4. P- and S-wave velocities as a function of differential pressure (loading and unloading processes) for samples TS1 (a), TS2 (b) and TS3 (c) at nitrogen gas and water-saturated conditions.

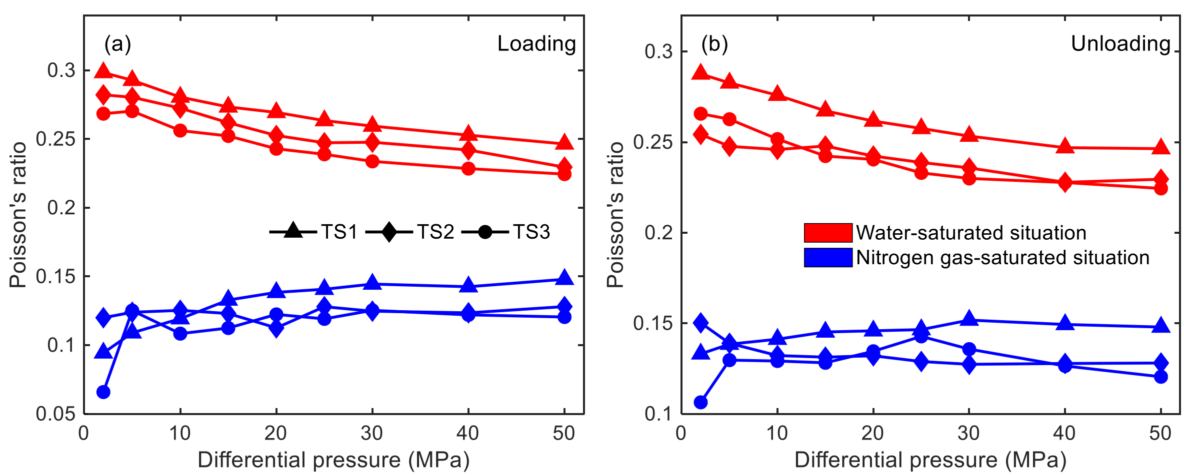

Fig. 5. Dynamic Poisson's ratio as a function of differential pressure for samples TS1, TS2 and TS3 at nitrogen gas and water saturation. (a) Loading processes, (b) unloading processes.

pressure was increased to 10 MPa. The latter was kept constant, while the former was increased (loading) with a stress rate of 0.1 MPa/min to a value of $P_c = 60$ MPa and decreased (unloading) at the same stress rate to $P_c = 12$ MPa. After reaching each pressure, the state was maintained for 2 h. Then, the ultrasonic P- and S-wave velocities were measured by the pulse-transmission technique with relative errors of $\pm 0.5\%$ and $\pm 1\%$, respectively.

(4) The dry samples were placed in a vacuum chamber filled with water, and evacuated for 2 h until there were no bubbles escaping from the surface of the specimens. We determined the full water-saturation state by comparing the weight of water (product of the pore volume and fluid density ρ_f) with that of the sample. Then, the samples were tested by using the same procedure as in step 3.

(5) Regarding the electrical-conductivity experiments with brine saturation, the samples were dried and placed in a vacuum chamber filled with the fluid containing 5% NaCl for 2 h. The conductivities were then measured at confining pressures of 5–35 MPa and a constant pore pressure of 0 MPa by using an impedance-capacitance-resistance meter. The relative error of the measurement was 0.5%.

(6) Regarding the strain measurements, the samples were washed, dried and placed in a static deformation unit, which includes the loading frame, confining pressure control, linear variable displacement transducers (LVDTs), strain gauges and internal load cell. The LVDTs are mounted between the endcaps to measure the axial strain, and the strain gauges are attached to the

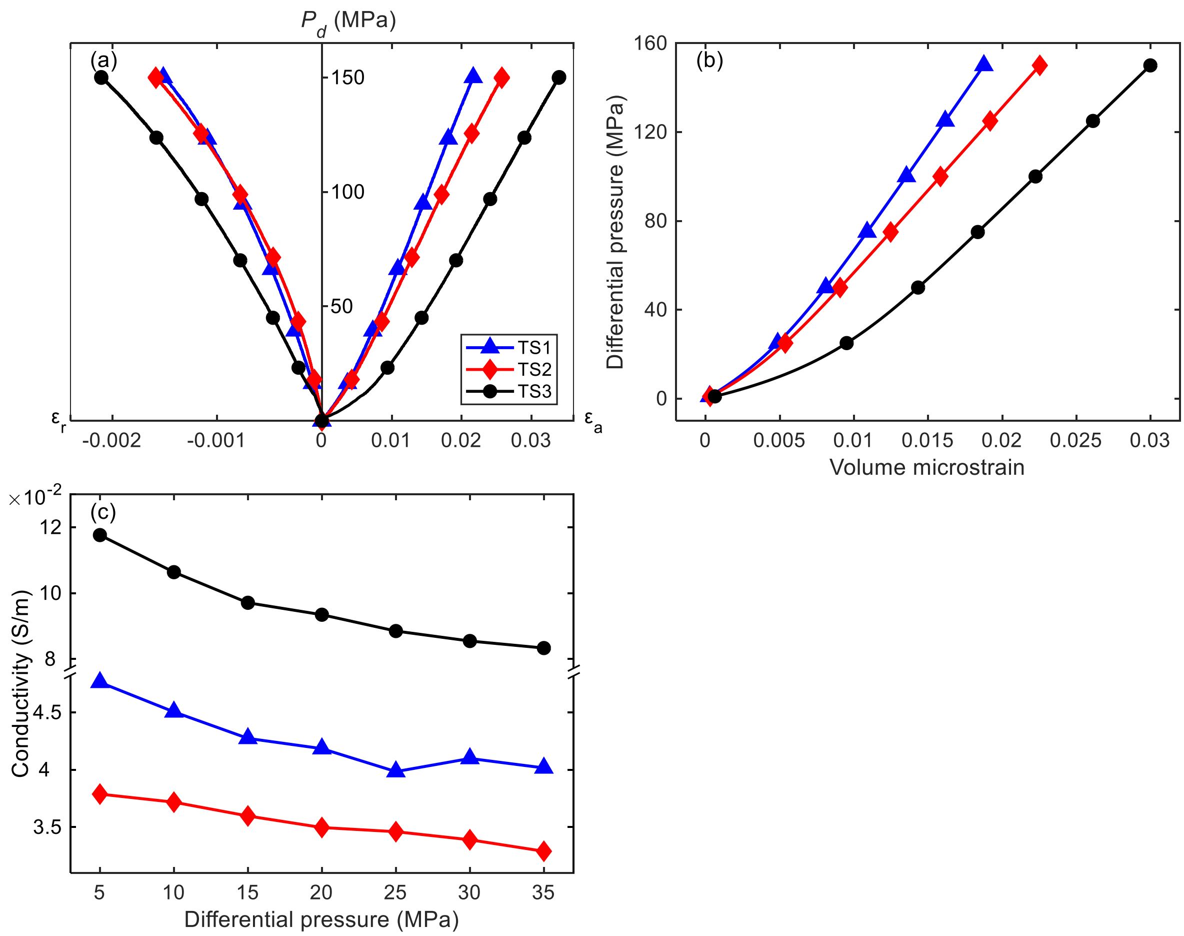

Fig. 6. (a) Axial (ε_a) and radial (ε_r) strains, (b) Volume microstrain and (c) Electrical conductivity as a function of the differential pressure for the TS1 (blue line with triangles), TS2 (red line with diamonds) and TS3 (black line with circles) samples. (For interpretation of the references to color in this figure legend, the reader is referred to the Web version of this article.)

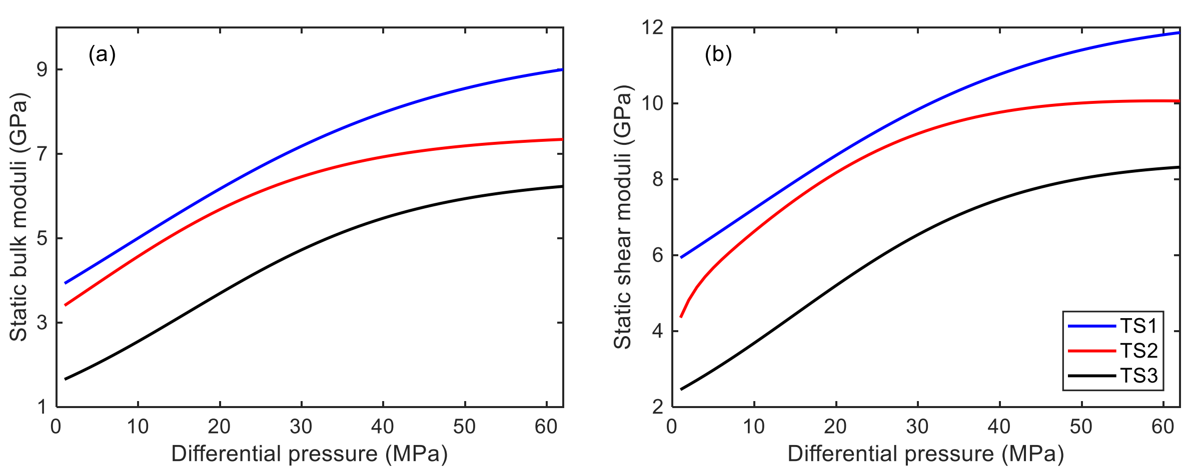

Fig. 7. Static bulk (a) and shear (b) moduli as a function of the differential pressure for the TS1 (blue line), TS2 (red line) and TS3 (black line) samples. (For interpretation of the references to color in this figure legend, the reader is referred to the Web version of this article.)

sample to measure the radial strain. When the axial force is exerted, the axial and circumferential stress-strain curves were measured at confining pressures of 0–150 MPa and a constant pore pressure of 0 MPa. The relative error of the measurements was less than 5%.

3. Results

3.1. Porosity and permeability

The porosities and permeabilities of the three samples as a function of differential pressure are shown in Fig. 2. For TS1, TS2 and TS3, these properties decrease nonlinearly at low differential pressures below 20,

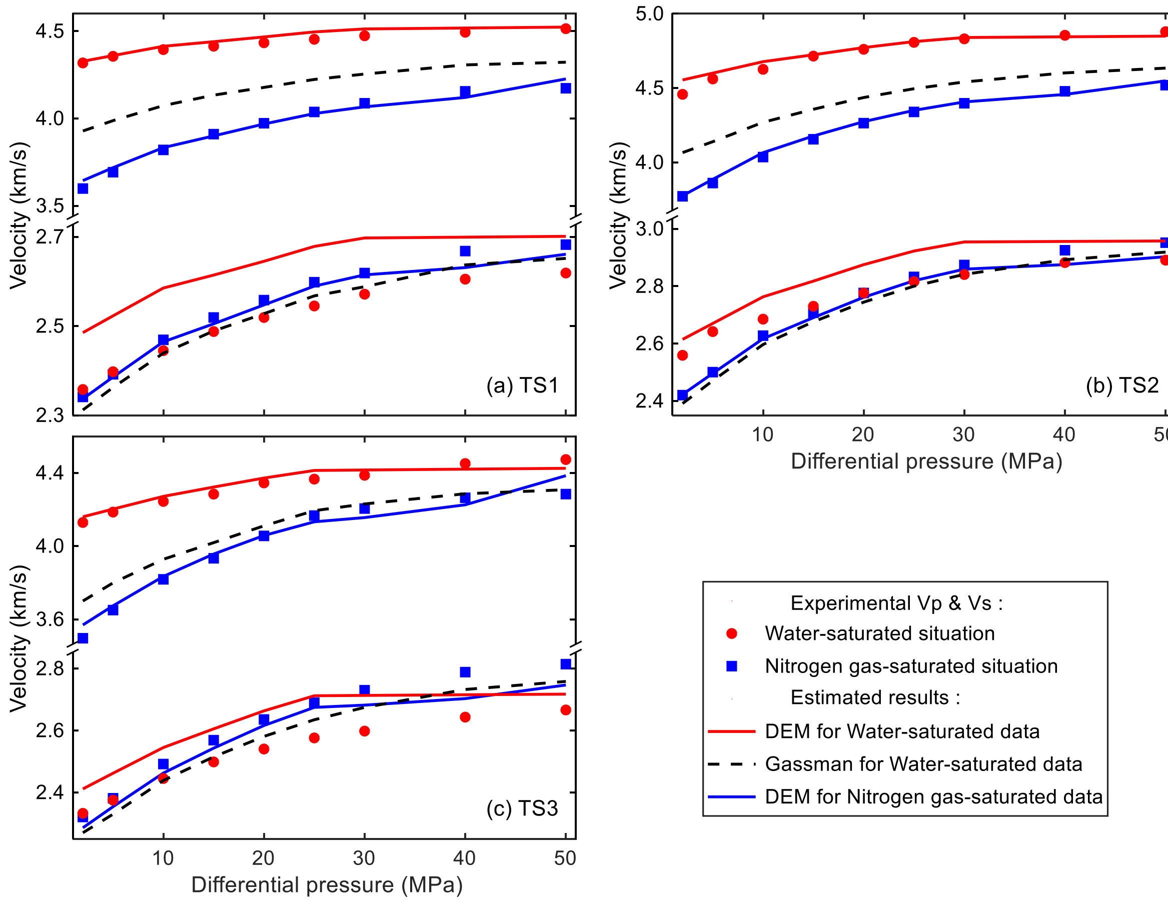

Fig. 8. Comparisons between the experimental and theoretical velocities for the TS1(a), TS2(b) and TS3(c) samples. The blue squares and red circles denote the experimental data at nitrogen gas and water-saturation conditions, respectively; the blue lines are the inversion results with the joint elastic-electrical inversion by using the static moduli; the red lines are the modeling results by using the pore aspect ratio spectrum (inverted with the joint elastic-electrical inversion) as an input in the DEM model, and the black broken lines denote the results obtained with Gassmann equation. (For interpretation of the references to color in this figure legend, the reader is referred to the Web version of this article.)

25 and 40 MPa, respectively, and then decrease linearly at higher pressures. This nonlinear behavior can be attributed to the closure of cracks with increasing pressure (Guéguen and Boutéca, 2004; Izumotani and Onozuka, 2013; Walsh, 1965; Watanabe et al., 2019). This behavior can be described by a dual-porosity concept, where the pore space can be partitioned into stiff pores and cracks (soft pores). The pressure dependences can be well approximated by linear and exponential terms (e.g., Pervukhina et al., 2010; Shapiro, 2003; Shapiro et al., 2015; Zhang et al., 2019a, 2020; Zheng et al., 2015; Zimmerman, 1991) (see Table 3). The results indicate that the best fit is obtained with a squared correlation coefficient $R^2 = 0.98$ (0.99), 0.95 (0.95) and 0.99 (0.99) for porosity (permeability).

3.2. Ultrasonic velocities

Ultrasonic waveforms are recorded at different conditions, and the first arrivals are picked with the method of Akram and Eaton (2016). As an example, Fig. 3 shows the P- and S-wave waveforms of the water-saturated TS3 sample at different differential pressures (loading and unloading processes). It is observed that the wave amplitude gradually increases with increasing differential pressure, while the first arrival time decreases. Then, we obtained the P (V_P) and S-(V_S) wave velocities corresponding to nitrogen gas and water as pore fluid as a function of the differential pressure (see Fig. 4). The behavior of the curves is nonlinear at low differential pressures and is ascribed to the closure of cracks. V_P for the nitrogen gas-saturated samples is lower than that corresponding to water, while V_S in both cases exhibits a 'crossover point' at some pressure, with V_S in the latter case being lower at high differential pressures. Similar results can be found in other works (e.g., Coyner, 1984; King, 1966; Yin et al., 2017). The increases in the velocities of the former case are larger than those of the latter case. The behavior is such that the fluid with higher elastic moduli may hinder the closure of cracks under loading. Additionally, hysteresis is observed between the loading and unloading processes, because some of the cracks with low aspect ratio close during the loading process and do not re-open under unloading. To minimize the hysteresis effect, the measurements of the unloading process are used for the modeling in the next sections.

The dynamic Poisson ratio as a function of the differential pressure can be obtained as $\nu_d = 1/2((V_p/V_S)^2 - 2)/((V_p/V_S)^2 - 1)$ (see Fig. 5). This ratio, when the fluid is nitrogen gas, varies between 0.05 and 0.15 in the whole differential pressure range, in agreement with the range for tight gas sandstones (0.05–0.2) provided by Al-Dughaimi et al. (2021). The value of the TS1 sample increases with increasing pressure, while two samples do not show variations, which may be related to the velocity measurements. This behavior can be related to the closure of cracks. For water-saturated conditions, ν_d is between 0.2 and 0.3, and decreases with pressure. Similar results can be found in other works (e.g., Pimienta et al., 2016; Toksöz et al., 1976; Wang et al., 2012).

3.3. Volume microstrain and electrical conductivity

Fig. 6 shows the axial ε_a and radial ε_r strains, volume microstrain ε_v and electrical conductivity for each sample. The ε_v is determined from

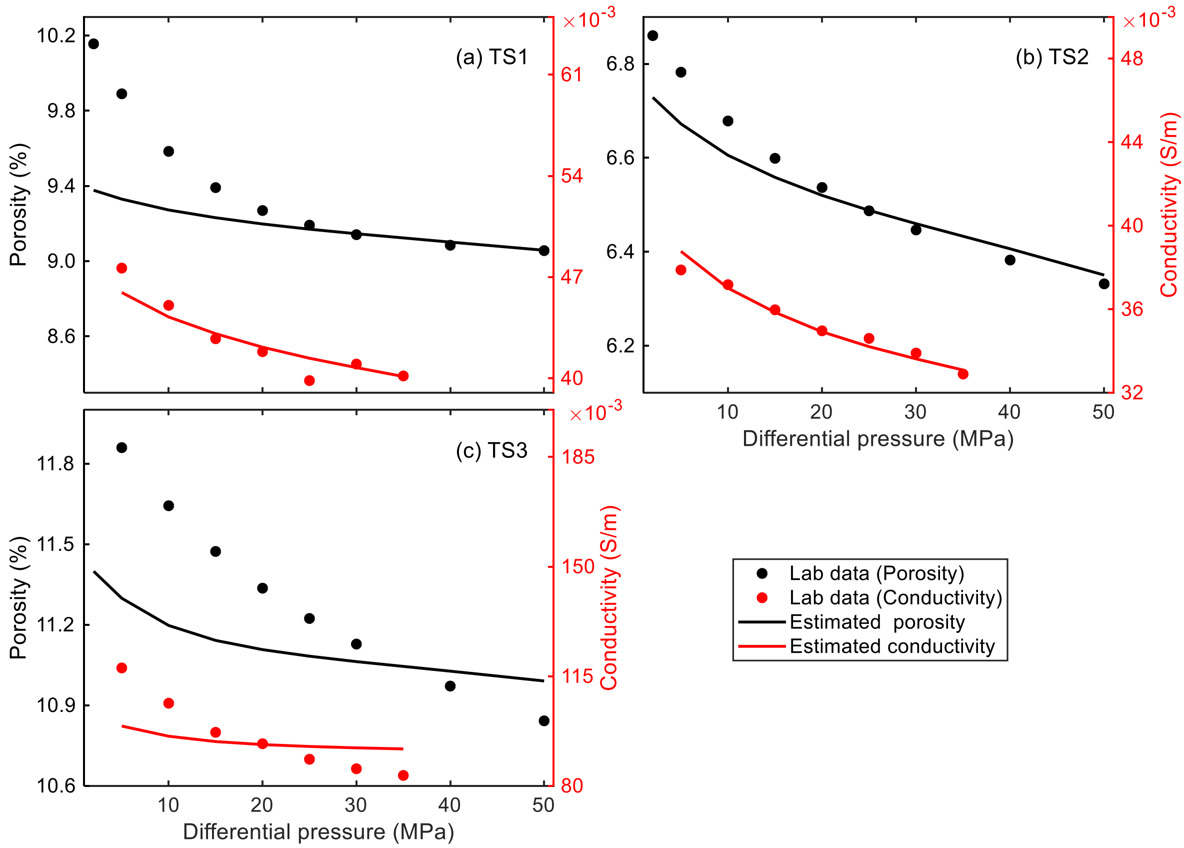

Fig. 9. Comparisons between the experimental and theoretical porosity and conductivity for the TS1(a), TS2(b) and TS3(c) samples. The black and red circles denote the measured porosity and conductivity, respectively, and the black and red lines are the corresponding results from the joint inversion using the static moduli. (For interpretation of the references to color in this figure legend, the reader is referred to the Web version of this article.)

$\varepsilon_v = \varepsilon_a + 2\varepsilon_r$. In Fig. 6a and b, ε_a (ε_r) and ε_v increase sharply and nonlinearly at low pressures, and then the behavior is linear. This nonlinear phenomenon is also related to the closure of cracks. At the same pressure, it is observed that the TS3 sample shows the highest ε_v, followed by the TS2 and TS1 samples. Similar to the case of porosity and permeability, the electrical conductivities of TS1 and TS2 decrease rapidly with increasing differential pressure at the low pressure range, and a gentle linear decrease is observed at high pressures, while the conductivity of TS3 is approximately linearly related to pressure.

4. Inversion of the unified pore geometry

4.1. Modeling

4.1.1. Multiphase R-DEM model

According to the R-DEM model (Cilli and Chapman, 2021), the relation between the elastic and electrical properties of a two-phase composite media and the pore geometry is given by

$$\frac{dK^*}{dc} = \frac{(K_i - K^*)P^{(*i)}}{(1-c)} \tag{1a}$$

$$\frac{d\mu^*}{dc} = \frac{(\mu_i - \mu^*)Q^{(*i)}}{(1-c)} \tag{1b}$$

and

$$\frac{d\sigma^*}{dc} = 3\sigma^* \frac{(\sigma_i - \sigma^*)R^{(*i)}}{(1-c)} \tag{2}$$

with the initial conditions $K^*(c=0) = K_g$, $\mu^*(c=0) = \mu_g$ and $\sigma^*(c=0) = \sigma_g$, where c is the inclusion volume fraction, K, μ and σ denote the bulk and shear moduli and electrical conductivity, respectively. Subscripts "g" and "i" represent the background (i.e., grains) and inclusion phases, respectively, while superscript "*" defines the effective properties of the rock. P, Q and R denote the geometric functions of the arbitrary spheroidal inclusions. The expressions of P and Q can be found in Berryman (1992), and that of R in Cilli and Chapman (2021).

To model the effects of multiple inclusion shapes or many constituents on the physical properties, the R-DEM model is extended to many phases, based on an incremental algorithm (Berg, 2007; Han, 2016). That is, the effective properties are treated as a new background or host medium in the next addition. By using equations (1) and (2) in each addition, we stop the additions when the desired pore geometry is reached (assumed to consist of a set of oblate spheroidal inclusions with different aspect ratios α_k ($k = 1, 2, \cdots, n$) and corresponding volume fraction c_k).

4.1.2. Pressure dependence

For an oblate inclusion with aspect ratio α, the volume fraction is given by $c(\alpha) = 4\pi r^3\alpha/3$, where r is the radius of the inclusion, and we assume it constant, i.e., we have $d\alpha/\alpha = dc(\alpha)/c(\alpha)$. The volume changes with differential pressure are given by Toksöz et al. (1976),

$$\frac{dc(\alpha)}{c(\alpha)} = -\frac{P_d/K_A^*}{E_1 - \frac{E_2E_3}{E_3+E_4}} \tag{3}$$

where K_A^* is the effective static bulk modulus of the dry rock, E_1-E_4 are functions of α and the effective matrix moduli $\widehat{K}_A$ and $\widehat{\mu}_A$ are defined as the effective static moduli of the rock with all the pores except those with aspect ratio α. These quantities are assumed to be the effective static moduli of the dry rock. To compute them, a high-order polynomial is used to fit the stress–strain curve. Then, the static bulk (K_s) and shear

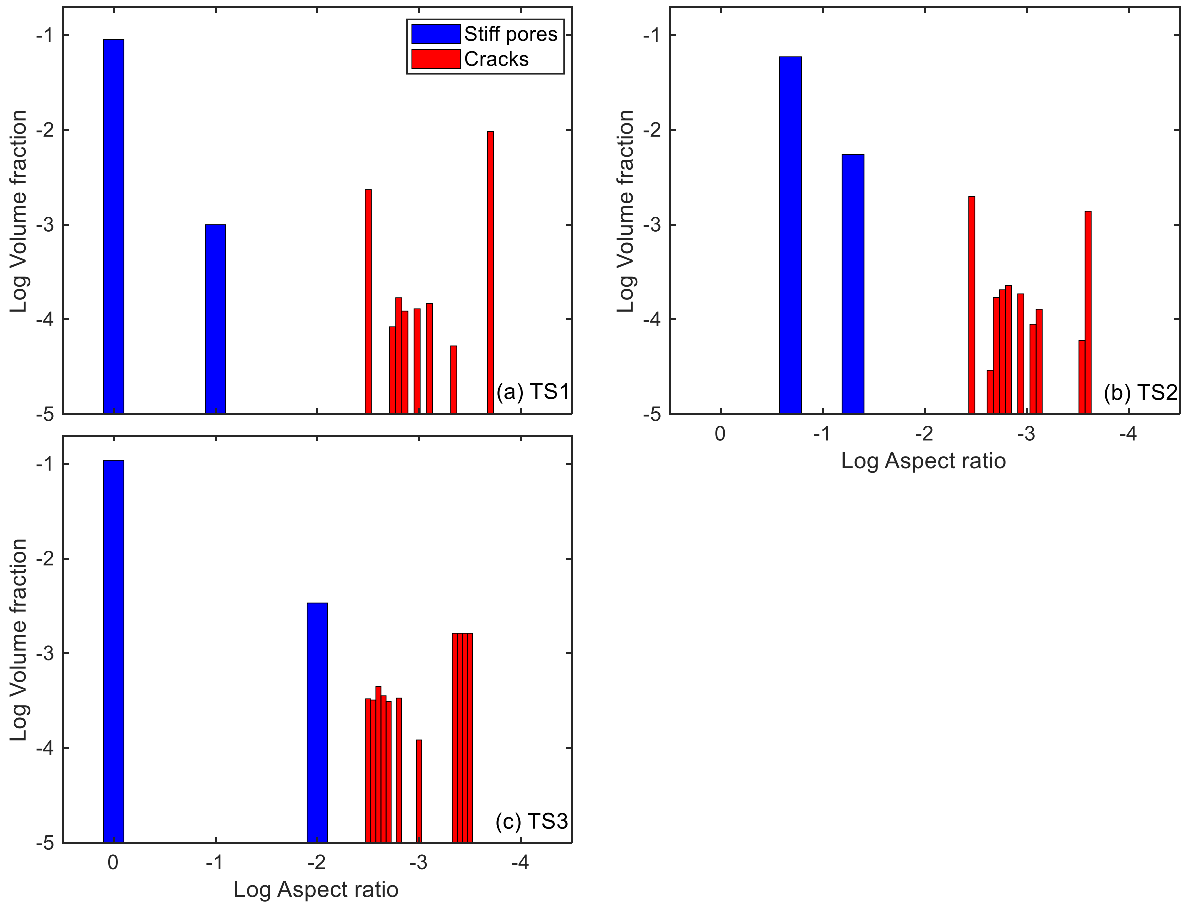

Fig. 10. Pore aspect ratio spectrum estimated by the joint inversion, based on the static moduli for the TS1(a), TS2(b) and TS3(c) samples.

Table 4
Squared correlation coefficients R^2 between theory and experiments from the joint inversion with the static moduli.

Sample	R^2 on $V_{P,Ng}$	R^2 on $V_{S,Ng}$	R^2 on $V_{P,sat}$	R^2 on $V_{S,sat}$	R^2 on φ	R^2 on σ
TS1	0.989	0.967	0.869	−0.414	0.117	0.871
TS2	0.993	0.978	0.917	0.461	0.853	0.942
TS3	0.996	0.971	0.977	0.039	0.121	0.345

(μ_s) moduli are estimated as $K_s = dP_d/d\varepsilon_v$and $\mu_s = 3K_s(1-2\nu_s)/(2+2\nu_s)$, where the static Poisson ratio is $\nu_s = -\varepsilon_r/\varepsilon_a$. The results are shown in Fig. 7 as a function of the differential pressure, where it is observed that the moduli increase rapidly at low pressures, and have a slow linear trend at high pressures. The nonlinear change of these moduli can also be ascribed to the closure of cracks.

The volume fraction and aspect ratio of a set of oblate inclusions (pores) at the l-th differential pressure $P_{d,l}$, is given by (Cheng, 1978)

$$c_{lk} = c_{0k}\left(1+\frac{\mathrm{d}c}{c}(\alpha_{0k}, P_{d,l})\right) \tag{4}$$

and

$$\alpha_{lk} = \alpha_{0k}\left(1+\frac{\mathrm{d}c}{c}(\alpha_{0k}, P_{d,l})\right) \tag{5}$$

respectively, where c_{0k} and α_{0k} are values at zero differential pressure. When $d\alpha/\alpha \le -1$, the oblate pore is nearly closed. The pore aspect ratio spectrum at any pressure can be estimated from equations (4) and (5).

4.1.3. Inversion algorithm

When the grain properties, static elastic moduli and pore aspect-ratio spectrum are known, the pressure-dependence of the velocities and electrical conductivity can be obtained from equations (1)–(5). Conversely, that spectrum can be inverted from the physical properties. In the inversion process, the experimental pressure-dependent porosity is a constraint (Yan et al., 2014) (it is resampled the porosity as a function of the pressure regarding the velocity measurements). Then, the mean square error between theory and experiment is quantified with the following objective function:

$$\begin{aligned} &F_{ela}(\alpha_{01}, \alpha_{02}, \cdots\alpha_{0n}, c_{01}, c_{02}, \cdots c_{0n}, K_g, \mu_g, \sigma_g) \\ &= \min\left[\sum_{l=1}^{L}\left(V_{Pl}^{m} - V_{Pl}^{DEM}\right)^2 + \sum_{l=1}^{L}\left(V_{Sl}^{m} - V_{Sl}^{DEM}\right)^2 + \sum_{l=1}^{L}\left(c_l^{m} - c_l^{p}\right)^2 + \sum_{l=1}^{L}\left(\sigma_l^{m} - \sigma_l^{DEM}\right)^2\right] \end{aligned} \tag{6}$$

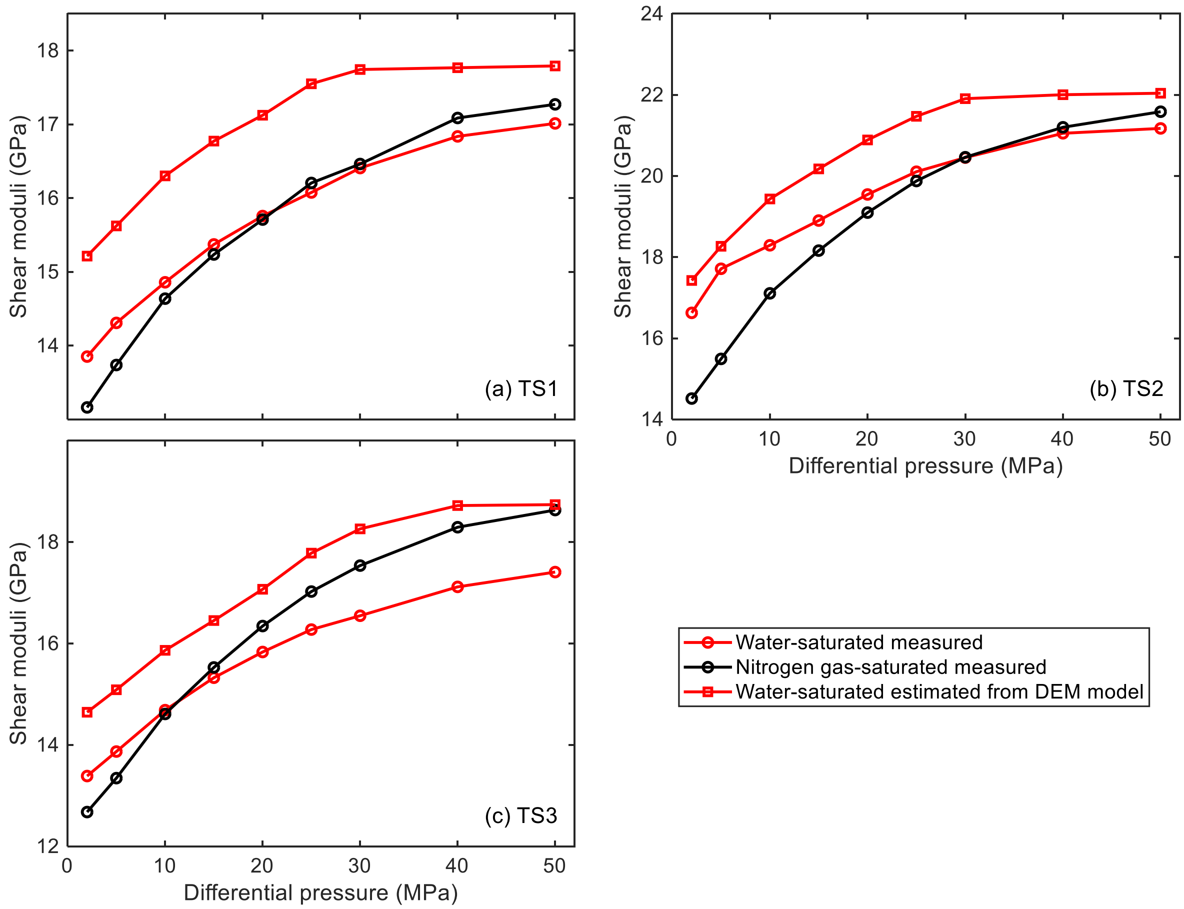

Fig. 11. Shear moduli as a function of the differential pressure for the TS1(a), TS2(b) and TS3(c) samples. The black and red lines with circles denote measurements under nitrogen gas and water saturation conditions, respectively, and the red lines with squares denotes the results of the DEM model. (For interpretation of the references to color in this figure legend, the reader is referred to the Web version of this article.)

where L is the number of differential pressures during the experiment, V_{Pl}^{m}, V_{Sl}^{m}, c_l^{m} and $\sigma_l^{m}$are the measured P- and S-wave velocities, porosity and electrical conductivity at the l-th differential pressure, respectively, and V_{Pl}^{DEM}, V_{Sl}^{DEM},c_l^{p} and σ_l^{DEM} are the predicted values. Then, the S and P velocities are $V_{Sl}^{DEM} = \sqrt{\mu^*/\rho}$ and $V_{Pl}^{DEM} = \sqrt{(K^* + 4/3\mu^*)/\rho}$, respectively, where $\rho = \rho_{dry} + \varphi\rho_f$ is the bulk density.

We adopt the very-fast-simulated annealing method to solve equation (6) (e.g., Ingber, 1989; Yamanaka, 2001), and to achieve optimal results, the aspect ratios are partitioned into those of stiff pores ($0.01 \leq \alpha \leq 1$) and those of cracks ($10^{-5} \leq \alpha < 0.01$), where the former can take any value between 0.01 and 1, while the latter is selected based on an equal log-normal spacing similar to that used by Izumotani and Onozuka (2013), Tao and King (1993) and Tran et al. (2008).

4.2. Pore geometry from the joint inversion using the static moduli

Because wave-induced local fluid flow affects the elastic properties of water-saturated rocks (e.g., Müller, et al., 2010; Ba et al., 2017), the estimated pore aspect ratio spectrum may be not reliable. Hence, the spectrum is inverted from the joint P- and S-wave velocities of the nitrogen gas-saturated samples ($V_{P,Ng}$ and $V_{S,Ng}$) and the electrical conductivity (σ) from the brine-saturated sample. Then, the result, input to equation (1), is used to estimate the velocities of the water-saturated rocks ($V_{P,sat}$ and $V_{S,sat}$). In addition, these are also estimated by using Gassmann's equations (Gassmann, 1951), where the dry-rock elastic moduli are obtained from of nitrogen gas-saturated samples by inverting Gassmann equation. The results for the three samples are shown in Figs. 8–10. The inverted bulk and shear moduli of the grains are respectively given by 30.74 and 25.54, 37.10 and 31.27, 28.73 and 25.72 GPa. The corresponding grain conductivities are determined to be 0.0274, 0.0225, and 0.0596 S/m, values that are higher than the conductivity of sand grains (0.01 S/m from Carcione et al., 2012), and significantly smaller than the conductivity of clay (0.2 S/m from Carcione et al., 2012). It is also noted that these estimated conductivities are positively correlated with the clay contents.

By comparing Figs. 8–10, it is shown that:

1. The joint modeling approach reasonably describes the pressure-dependent velocities, porosity and electrical conductivity. The squared correlation coefficients R^2 of the measured and predicted values are presented in Table 4. The R^2 of the velocities are higher than those of porosity and electrical conductivity, indicating that the predicted velocities better approach the measurements than the estimated porosity and electrical conductivity. In addition, the modeling results of TS2 are better than those of TS1 and TS3, suggesting that the estimated pore geometry of TS2 is better. It indicates that the multiphase R-DEM model have the capability of jointly modeling elastic wave velocities and electrical conductivity for TS1 and TS2 samples, while the estimated conductivity of the TS3 sample is not so good, probably because cracks are well developed in this sample (see Fig. 1e and f). The discrepancies between the theory and measurements could be associated with the fact that the assumption of oblate spheroidal inclusions cannot properly describe the pore shapes of real rocks. In addition, this could also be related to the presence of clay according to the work of Burns et al. (1990).

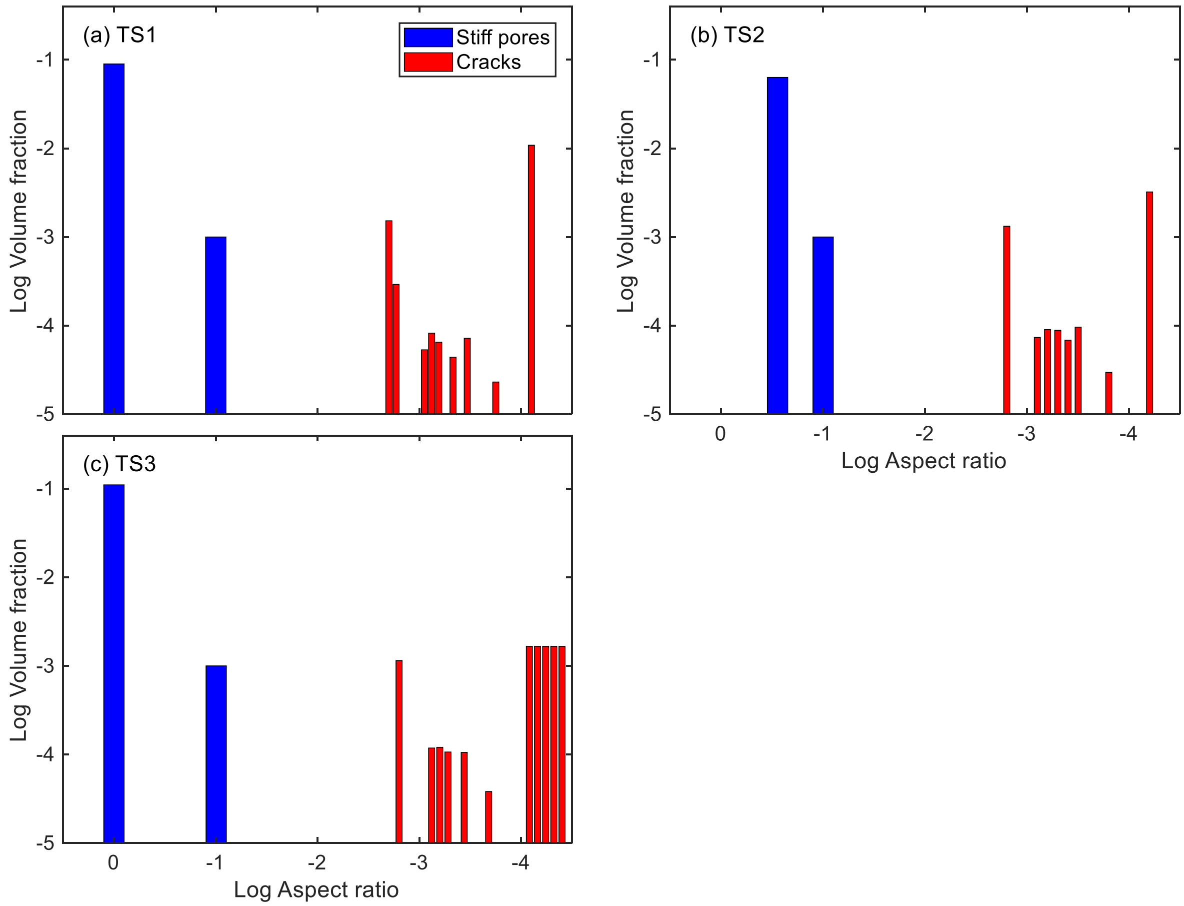

Fig. 12. Pore aspect ratio spectra obtained with the joint inversion, based on the dynamic moduli for the TS1(a), TS2(b) and TS3(c) samples.

Table 5
Squared correlation coefficients R^2 between theory and experiments from the joint inversion with the dynamic moduli.

Sample	R^2 on $V_{P,Ng}$	R^2 on $V_{S,Ng}$	R^2 on $V_{P,sat}$	R^2 on $V_{S,sat}$	R^2 on φ	R^2 on σ
TS1	0.977	0.980	0.813	−1.003	−0.132	0.739
TS2	0.994	0.979	0.912	0.402	0.342	0.916
TS3	0.966	0.926	0.904	0.171	0.014	0.212

2. $V_{P,sat}$ estimated from the Gassmann equation is lower than the measurements, and the difference decreases with pressure. Similar results were reported in previous experimental studies (Adelinet et al., 2011; Agersborg et al., 2008; David and Zimmerman, 2012; King et al., 2000; King and Marsden, 2002; Zhang et al., 2019b). In contrast, the results obtained from the DEM model are in better in agreement with the experimental data of water-saturated rocks, suggesting that this model, with a unified pore geometry obtained with the joint inversion, can be used in this case. The water-saturated samples are in an unrelaxed regime, which can be described by a critical frequency of the local fluid flow between pores and cracks, i.e., $f_c = \alpha_{max}^3 K_g/\eta_w$ (O'Connell and Budiansky, 1977), where α_{max} is the maximum crack aspect ratio of the spectrum, and water viscosity η_w is 0.001 Pa·s. For the TS1, TS2 and TS3 samples, the values of α_{max} are 0.00294, 0.00321 and 0.00267 at $P_d = 2$ MPa, and the critical frequencies are approximately equal to 0.78, 1.2 and 0.54 MHz, respectively. Water is trapped in the individual pores or cracks during the ultrasonic measurement process ($f = 0.5$ MHz). The predictions of the DEM model can provide an upper bound for the elastic moduli. Similar discussions were presented in David and Zimmerman. (2012).
3. For V_S, the estimations with the Gassmann equation are lower than the measurements for the nitrogen-saturated rocks ($V_{S,Ng}$), which is related to a fluid-density effect. There is a crossover point between the predictions and measurements for water-saturated rocks ($V_{S,sat}$), which can be related to the combined effects of fluid density, and shear stiffening and weakening. Previous studies showed that the shear-stiffening effect is associated with the presence of cracks (David et al., 2013; David and Zimmerman, 2012; Shafiro and Kachanov, 1997), and the shear-weakening one (a chemical reaction between fluid and solid phases) can be due to the presence of clay minerals (Clark et al., 1980; Khazanehdari and Sothcott, 2003; Pimienta et al., 2014b). To analyze both effects, Fig. 11 shows the shear moduli derived from ultrasonic S-wave velocities and the corresponding densities under nitrogen-gas and water saturation conditions. Those corresponding to water are higher than those of nitrogen gas at low differential pressures, suggesting that the shear-stiffening effect is more significant than the shear-weakening one. At low differential pressures, a large number of open cracks are present. Since cracks close at increasing pressure, both the shear stiffening and weakening effects decrease (Khazanehdari and Sothcott, 2003; Yin et al., 2019). However, the decrease of the former is more pronounced. This explains why the measured shear moduli of water-saturated rocks is lower than those of the nitrogen gas-saturated ones at high differential pressures. Fig. 11 shows that the results obtained with the DEM model are higher than the experimental data for water-saturated rocks. The shear stiffening and weakening effects lead to the misfits between the Gassmann equation and DEM model and experimental data.

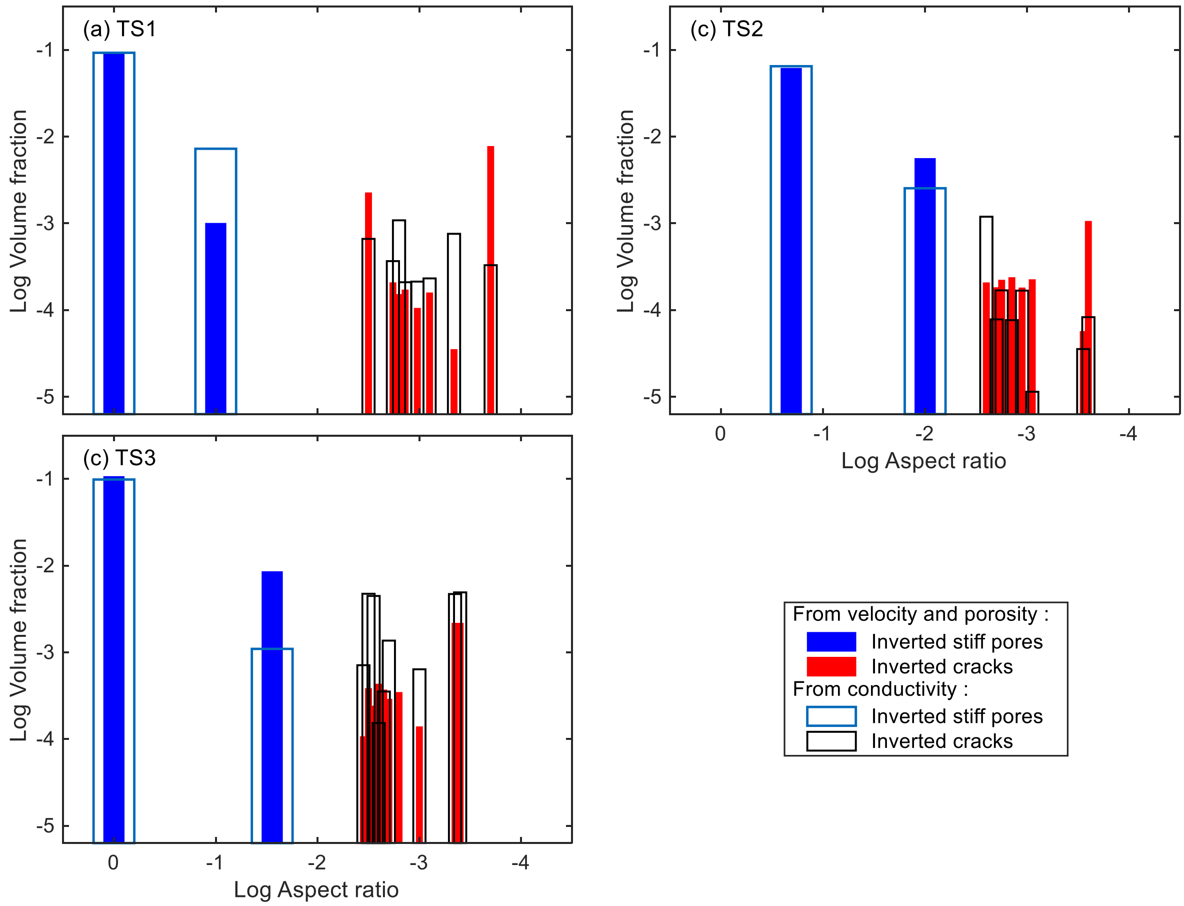

Fig. 13. Pore aspect ratio spectra estimated from unjoint elastic and electrical inversions, based on the static moduli for the TS1(a), TS2(b) and TS3(c) samples.

Table 6
Squared correlation coefficients R^2 between theory and experiments from the unjoint inversion, based on the static moduli.

Sample	R^2 on $V_{P,Ng}$	R^2 on $V_{S,Ng}$	R^2 on $V_{P,sat}$	R^2 on $V_{S,sat}$	R^2 on φ	R^2 on σ
TS1	0.985	0.937	0.713	−0.143	0.454	0.972
TS2	0.994	0.986	0.940	0.309	0.885	0.985
TS3	0.990	0.985	0.934	0.121	0.531	0.998

4. In the pore aspect ratio spectrum at zero differential pressure, the first two represent stiff pores, while the remaining ones are cracks. For samples TS1, TS2 and TS3, the pores with aspect ratio of 1, 0.2 and 1 dominate, and the crack aspect ratios are in the range of 0.00316–0.0002, 0.00347–0.00025 and 0.00316–0.00032, respectively. It is noted that the distribution of crack aspect ratios in TS1 are slightly wider compared to the other two samples, and there is a distinct peak in the spectrum of TS1 at the smallest one (0.0002). The histograms suggest that these cracks will sharply approach closure with increasing pressure, which explains why the nonlinear range of the measured porosity and permeability of TS1 is narrow (see Fig. 2). In addition, the crack porosities (the sum of the volume fractions of all cracks at zero differential pressure) estimated with the joint inversion are 0.0127, 0.00448 and 0.00876 for the three samples, which are almost consistent with the values estimated from the measured porosity (See Table 2).

4.3. Pore geometry from the joint inversion with the dynamic moduli

Since K_A^*, $\widehat{K}_A$ and $\widehat{\mu}_A$ are not known or measured, they are usually considered to be equal to the effective dynamic moduli of the dry rock (Cheng and Toksöz, 1979; Izumotani and Onozuka, 2013; Yan et al., 2014; Tang et al., 2021), which are obtained from the measurements on the nitrogen gas-saturated samples by inverting the Gassmann equation. To analyze the differences, the aspect ratio spectra obtained from the joint inversion, using the dynamic moduli, are given in Fig. 12. The estimated bulk (shear) moduli and conductivities of the grains are 31.22 (27.2) GPa and 0.0277 S/m, 35 (32) GPa and 0.023 S/m, and 28.68 (27.23) GPa and 0.0636 S/m for the TS1, TS2 and TS3 samples, respectively. These grain properties are close to those listed in Section 4.2. It is shown that the crack aspect ratios at zero differential pressure are in the ranges 0.0017–0.00008, 0.00158–0.00006 and 0.00158–0.00004 for TS1, TS2 and TS3, respectively. Unlike Fig. 10, cracks with low aspect ratio are significant in the results, because the dynamic moduli are generally higher than the static ones, and then the rate of crack closure is lower. Hence, only when cracks have a small aspect ratio, the modeling with the dynamic moduli reasonably agrees with the data. It also indicates that the aspect ratio spectra obtained from the dynamic moduli underestimates the true ones. Similar discussions can be found in Cheng and Toksöz (1979). The squared correlation coefficients R^2 of the measured and predicted values are presented in Table 5, where the estimated spectra in this section, input to equation (1), are used to calculate the velocities of water-saturated rocks. Compared with Table 4, the results obtained with the static moduli are better. Moreover, the estimated crack porosities are 0.013, 0.005 and 0.01 for the three samples, which are slightly higher than the values estimated with the measured porosities (See Table 2).

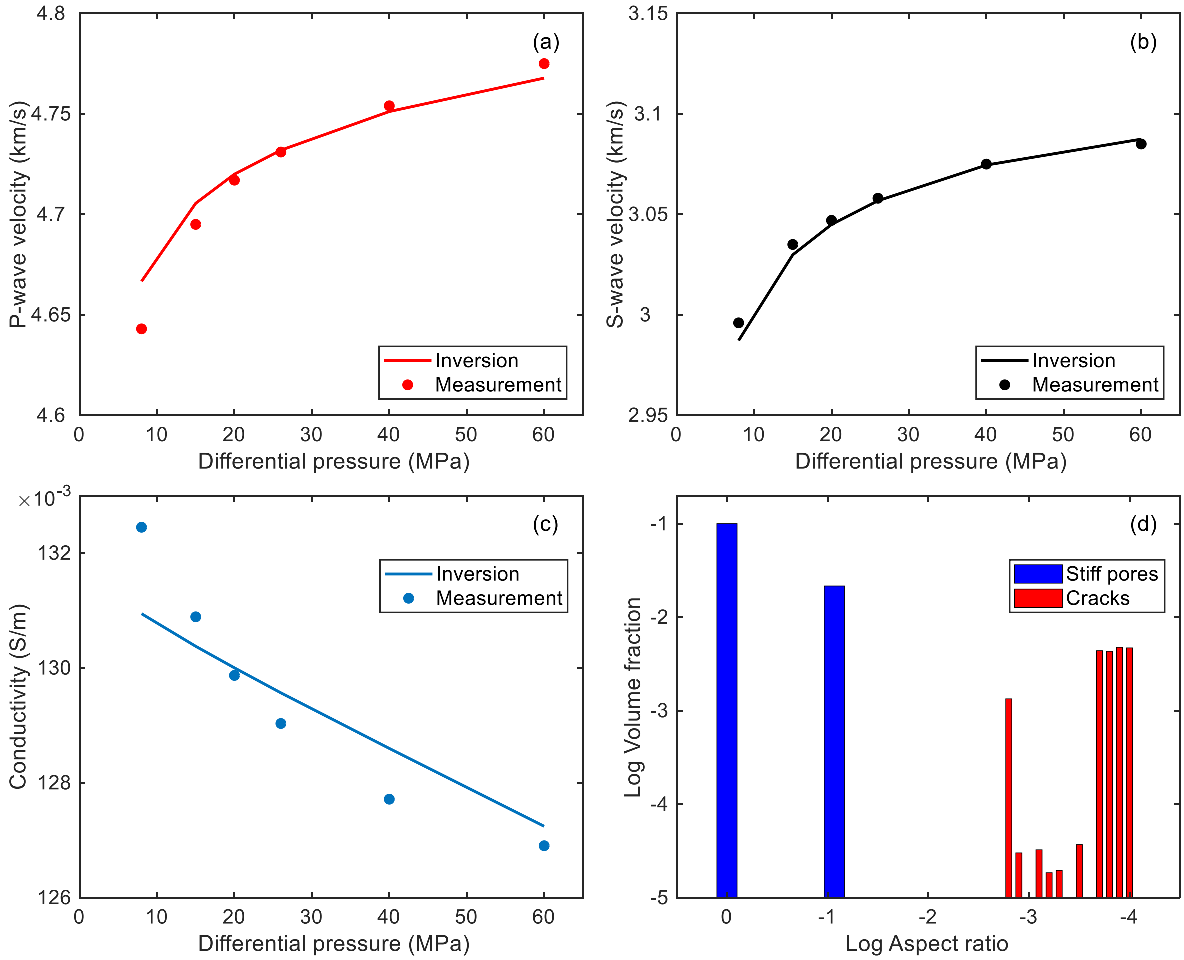

Fig. 14. Joint inversion for the clean sandstone E4. (a) P-wave velocity, (b) S-wave velocity, (c) electrical conductivity, and (d) estimated pore aspect ratio spectra. The solid lines are the modeling results according to the multiphase R-DEM model and the circles denote the measurements by Han et al. (2011).

4.4. Pore geometry estimated from unjoint elastic and electrical inversions, based on the static moduli

In this section, we consider independent (unjoint) inversions, based on the static moduli. Fig. 13 shows the results. The grain properties of the three samples are consistent with the values of Section 4.2. For each sample, the estimated pore aspect ratios with different properties are almost the same, while there are differences between the volume fractions, other than that of pores with highest aspect ratio. Although the fluid-filled pores are added into the host medium in the same way as in the elastic modeling, the discrepancy between the pore aspect ratio spectra is present. The volume fractions of cracks for the TS3 sample obtained by electrical inversion are higher than those estimated by elastic inversion. Similar conclusions are given in Han et al. (2016), while the results of the other samples do not exhibit such behavior. The squared correlation coefficients R^2 are given in Table 6, where the estimated pore aspect ratio spectrum from the elastic inversion, input to equation (1), is used to estimate the velocities of the water-saturated samples. Although the unjoint results are better than the joint ones (compare with Table 4), it is seen that the estimated pore aspect ratio spectra significantly differ (compare Figs. 10 and 13). The results indicate that the pore geometry inverted with one physical property may fail to predict the other physical property.

4.5. Inversion by using published data

To further check the proposed model, we apply it to the reported measurements of ultrasonic velocity and electrical conductivity of a clean sandstone (E4) (Han et al., 2011), used by Han et al. (2016) to test a joint inversion with the SC model. These authors state: "Therefore, these SC models are not suitable for the joint elastic-electrical modeling of reservoir rocks, at least as currently configured. This argument is further strengthened by the large misfit (see Fig. 5) between the measured and the computed elastic and electrical properties based on the joint elastic-electrical inversion using a combination of equations (6) and (7) as the cost function". On the other hand, the proposed model performs quite well with a squared correlation coefficient R^2 of 0.933, 0.976 and 0.822 for V_P, V_S and σ, respectively (see Fig. 14). In the modeling, the values of K_A^*, $\widehat{K}_A$ and $\widehat{\mu}_A$ are approximated with the dynamic moduli of the dry rock, which are estimated from wet-rock measurements using Gassmann equation. The estimated bulk (shear) modulus and electrical conductivity of the grains are 35 (45) GPa and 0.0792 S/m, respectively. These values are different from those provided by Han et al. (2016) (35.7 (44) GPa and 0.03S/m). This is due to the different order with which the components are added in the SC and DEM models.

5. Conclusions

We have developed a novel elastic-electrical multiphase R-DEM theory (reformulated differential effective-medium) to model the physical properties of rocks (elastic velocity and electrical conductivity) and estimate a unified pore geometry, i.e., pore/crack with different aspect ratios and volume fractions. To test the model, we performed experiments on tight-sandstone samples to measure those properties as a function of the different differential pressure. The comparison between theory and experiment indicates that the theory shows a good performance, and that the inversion of the unified pore geometry by using the static stiffness modulus is more appropriate than the dynamic one. On the other hand, an unjoint modeling yields different pore geometries, confirming the use of the joint approach. Moreover, an application of the model to a clean sandstone is more successful than the use of the self-consistent theory. However, this does not mean that it can be applied to all clastic rocks and lithologies, but the model can easily be reformulated by adapting the theory to the specific case. Moreover, the estimated unified pore geometry can be used to estimate other physical properties, such as permeability and thermal conductivity.

Funding

This work is partially funded by the National Natural Science Foundation of China (42104110, 41974123, 42174161), Natural Science Foundation of Jiangsu Province (BK20210379). Jiangsu Innovation and Entrepreneurship Plan, Jiangsu Province Science Fund for Distinguished Young Scholars, and SINOPEC Key Laboratory of Geophysics.

Author statement

Lin Zhang: Methodology, Validation, Writing- Original draft preparation. Jing Ba: Conceptualization, Supervision, Funding acquisition, Writing- Reviewing. Chao Li: Investigation, Visualization. José M. Carcione: Supervision, Writing- Reviewing. Feng Zhou: Data curation, Formal analysis.

Declaration of competing interest

The authors declare that they have no known competing financial interests or personal relationships that could have appeared to influence the work reported in this paper.

Data availability

Data will be made available on request.

References

Adelinet, M., Dorbath, C., Le Ravalec, M., Fortin, J., Guéguen, Y., 2011. Deriving microstructure and fluid state within the Icelandic crust from the inversion of tomography data. Geophys. Res. Lett. 38 (3) https://doi.org/10.1029/2010GL046304.

Agersborg, R., Johansen, T.A., Jakobsen, M., Sothcott, J., Best, A., 2008. Effects of fluids and dual-pore systems on pressure-dependent velocities and attenuations in carbonates. Geophysics 73 (5), N35–N47. https://doi.org/10.1190/1.2969774.

Akram, J., Eaton, D.W., 2016. A review and appraisal of arrival-time picking methods for downhole microseismic data. Geophysics 81 (2), KS71–KS91. https://doi.org/10.1190/geo2014-0500.1.

Al-Dughaimi, S., Muqtadir, A., Alzaki, T., Dvorkin, J., 2021. Stress dependence of elastic and transport properties in tight gas sandstones. J. Petrol. Sci. Eng. 196, 108001 https://doi.org/10.1016/j.petrol.2020.108001.

Al-Wardy, W., Zimmerman, R.W., 2004. Effective stress law for the permeability of clay-rich sandstones. J. Geophys. Res. Solid Earth 109 (B4). https://doi.org/10.1029/2003JB002836.

Amalokwu, K., Falcon-Suarez, I.H., 2021. Effective medium modeling of pressure effects on the joint elastic and electrical properties of sandstones. J. Petrol. Sci. Eng. 202, 108540 https://doi.org/10.1016/j.petrol.2021.108540.

Aquino-López, A., Mousatov, A., Markov, M., 2011. Model of sand formations for joint simulation of elastic moduli and electrical conductivity. J. Geophys. Eng. 8 (4), 568–578. https://doi.org/10.1088/1742-2132/8/4/009.

Aquino-López, A., Mousatov, A., Markov, M., Kazatchenko, E., 2015. Modeling and inversion of elastic wave velocities and electrical conductivity in clastic formations with structural and dispersed shales. J. Appl. Geophys. 116, 28–42. https://doi.org/10.1016/j.jappgeo.2015.02.013.

Ba, J., Xu, W., Fu, L.Y., Carcione, J.M., Zhang, L., 2017. Rock anelasticity due to patchy saturation and fabric heterogeneity: a double double-porosity model of wave propagation. J. Geophys. Res. Solid Earth 122 (3), 1949–1976. https://doi.org/10.1002/2016JB013882.

Benveniste, Y., 1987. A new approach to the application of Mori-Tanaka's theory in composite materials. Mech. Mater. 6 (2), 147–157. https://doi.org/10.1016/0167-6636(87)90005-6.

Berg, C., 2007. An effective medium algorithm for calculating water saturations at any salinity or frequency. Geophysics 72 (2), E59–E67. https://doi.org/10.1190/1.2432261.

Berge, P.A., Berryman, J.G., Bonner, B.P., 1993. Influence of microstructure on rock elastic properties. Geophys. Res. Lett. 20 (23), 2619–2622. https://doi.org/10.1029/93GL03131.

Berryman, J.G., 1992. Single-scattering approximations for coefficients in Biot's equations of poroelasticity. J. Acoust. Soc. Am. 91 (2), 551–571. https://doi.org/10.1121/1.402518.

Berryman, J.G., 1995. Mixture theories for rock properties. Rock physics and phase relations: A handbook of physical constants 3, 205–228.

Bruggeman, V.D., 1935. Berechnung verschiedener physikalischer Konstanten von heterogenen Substanzen. I. Dielektrizitätskonstanten und Leitfähigkeiten der Mischkörper aus isotropen Substanzen. Ann. Phys. 416 (7), 636–664. https://doi.org/10.1002/andp.19354160705.

Bruner, W.M., 1976. Comment on 'Seismic velocities in dry and saturated cracked solids' by Richard J. O'Connell and Bernard Budiansky. J. Geophys. Res. 81 (14), 2573–2576. https://doi.org/10.1029/JB081i014p02573.

Burns, D.R., Cheng, C.H., Wilkens, R.H., 1990. Sandstone pore aspect ratio spectra from direct observations and velocity inversion. Int. J. Rock Mech. Min. Sci. Geomech. Abstracts 21 (4), 315–323. http://hdl.handle.net/1721.1/75073.

Carcione, J.M., 2022. Wave Fields in Real Media. Theory and Numerical Simulation of Wave Propagation in Anisotropic, Anelastic, Porous and Electromagnetic Media. Elsevier (Fourth edition, extended and revised).

Carcione, J.M., Gei, D., Picotti, S., Michelini, A., 2012. Cross-hole electromagnetic and seismic modeling for CO^2 detection and monitoring in a saline aquifer. J. Petrol. Sci. Eng. 100, 162–172. https://doi.org/10.1016/j.petrol.2012.03.018.

Carcione, J.M., Seriani, G., Gei, D., 2003. Acoustic and electromagnetic properties of soils saturated with salt water and NAPL. J. Appl. Geophys. 52, 177–191. https://doi.org/10.1016/S0926-9851(03)00012-0.

Cheng, C.H., 1978. Seismic velocities in porous rocks-Direct and inverse problems. Massachusetts Institute of Technology. ScD thesis.

Cheng, C.H., Toksöz, M.N., 1979. Inversion of seismic velocities for the pore aspect ratio spectrum of a rock. J. Geophys. Res. Solid Earth 84 (B13), 7533–7543. https://doi.org/10.1029/JB084iB13p07533.

Cheng, W., Carcione, J.M., Qadrouh, A., Alajmi, M., Ba, J., 2020a. Rock Anelasticity, Pore Geometry and the Biot-Gardner Effect, Rock Mechanics and Rock Engineering. https://doi.org/10.1007/s00603-020-02155-7.

Cheng, W., Carcione, J.M., Picotti, S., Ba, J., 2020b. Effect of pressure and fluid on pore geometry and anelasticity of dolomites. Rheol. Acta 59, 707–716. https://doi.org/10.1007/s00397-020-01231-7.

Clark, V.A., Tittmann, B.R., Spencer, T.W., 1980. Effect of volatiles on attenuation (Q-1) and velocity in sedimentary rocks. J. Geophys. Res. Solid Earth 85 (B10), 5190–5198. https://doi.org/10.1029/JB085iB10p05190.

Cilli, P., Chapman, M., 2018. Modelling the Elastic and Electrical Properties of Rocks with Complex Pore Geometries: 80th Annual International Conference and Exhibition, EAGE, Extended Abstracts.

Cilli, P.A., Chapman, M., 2021. Linking elastic and electrical properties of rocks using cross-property DEM. Geophys. J. Int. 225 (3), 1812–1823. https://doi.org/10.1093/gji/ggab046.

Cosenza, P., Camerlynck, C., Tabbagh, A., 2003. Differential effective medium schemes for investigating the relationship between high-frequency relative dielectric permittivity and water content of soils. Water Resour. Res. 39 (9) https://doi.org/10.1029/2002WR001774.

Coyner, K.B., 1984. Effects of Stress, Pore Pressure, and Pore Fluids on Bulk Strain, Velocity, and Permeability in Rocks. Doctoral dissertation, Massachusetts Institute of Technology.

David, E.C., Fortin, J., Schubnel, A., Guéguen, Y., Zimmerman, R.W., 2013. Laboratory measurements of low-and high-frequency elastic moduli in Fontainebleau sandstone. Geophysics 78 (5), D369–D379. https://doi.org/10.1190/geo2013-0070.1.

David, E.C., Zimmerman, R.W., 2012. Pore structure model for elastic wave velocities in fluid-saturated sandstones. J. Geophys. Res. Solid Earth 117 (B7). https://doi.org/10.1029/2012JB009195.

Eshelby, J.D., 1957. The determination of the elastic field of an ellipsoidal inclusion, and related problems. Proc. R. Soc. London, A 241 (1226), 376–396. https://doi.org/10.1098/rspa.1957.0133.

Fortin, J., Guéguen, Y., Schubnel, A., 2007. Effects of pore collapse and grain crushing on ultrasonic velocities and Vp/Vs. J. Geophys. Res. Solid Earth 112 (B8). https://doi.org/10.1029/2005JB004005.

Garnett, J.C.M., 1904. Colours in metal glasses and in metallic films. Phil. Trans. Roy. Soc. Lond. 203, 385–420. https://doi.org/10.1098/rsta.1904.0024.

Garnett, J.C.M., 1906. Colours in metal glasses, in metallic films, and in metallic solutions. II. Philos. Trans. R. Soc. London, Ser. A 205, 237–288. https://doi.org/10.1098/rsta.1906.0007.

Gassmann, F., 1951. Über die elastizität poröser medien: vier. der Natur. Gesellschaft Zurich 96, 1–23.

Gelius, L.J., Wang, Z., 2008. Modelling production caused changes in conductivity for a siliciclastic reservoir: a differential effective medium approach. Geophys. Prospect. 56 (5), 677–691. https://doi.org/10.1111/j.1365-2478.2008.00720.x.

Gomez, C.T., Dvorkin, J., Vanorio, T., 2010. Laboratory measurements of porosity, permeability, resistivity, and velocity on Fontainebleau sandstones. Geophysics 75 (6), E191–E204. https://doi.org/10.1190/1.3493633.

Guéguen, Y., Boutéca, M., 2004. Mechanics of Fluid-Saturated Rocks. Academic Press, New York.
Guéguen, Y., Schubnel, A., 2003. Elastic wave velocities and permeability of cracked rocks. Tectonophysics 370 (1–4), 163–176. https://doi.org/10.1016/S0040-1951(03)00184-7.
Han, T., 2016. A simple way to model the pressure dependency of rock velocity. Tectonophysics 675, 1–6. https://doi.org/10.1016/j.tecto.2016.03.008.
Han, T., 2018. Joint elastic-electrical properties of artificial porous sandstone with aligned fractures. Geophys. Res. Lett. 45 (7), 3051–3058. https://doi.org/10.1002/2018GL077541.
Han, T., Best, A.I., Sothcott, J., MacGregor, L.M., 2011. Pressure effects on the joint elastic-electrical properties of reservoir sandstones. Geophys. Prospect. 59 (3), 506–517. https://doi.org/10.1111/j.1365-2478.2010.00939.x.
Han, T., Clennell, M.B., Cheng, A.C., Pervukhina, M., 2016. Are self-consistent models capable of jointly modeling elastic velocity and electrical conductivity of reservoir sandstones? Geophysics 81 (4), D377–D382. https://doi.org/10.1190/geo2015-0690.1.
Han, T., Clennell, M.B., Josh, M., Pervukhina, M., 2015. Determination of effective grain geometry for electrical modeling of sedimentary rocks. Geophysics 80 (4), D319–D327. https://doi.org/10.1190/geo2014-0504.1.
Han, T., Wei, Z., Li, F., 2020. How the effective pore and grain shapes are correlated in Berea sandstones: implications for joint elastic-electrical modeling. Geophysics 85 (3), MR147–MR154. https://doi.org/10.1190/geo2019-0756.1.
Ingber, L., 1989. Very fast simulated re-annealing. Math. Comput. Model. 12 (8), 967–973. https://doi.org/10.1016/0895-7177(89)90202-1.
Izumotani, S., Onozuka, S., 2013. Elastic moduli and the aspect ratio spectrum of rock using simulated annealing. Geophys. Prospect. 61, 489–504. https://doi.org/10.1111/1365-2478.12003.
Kachanov, M., 1993. Elastic solids with many cracks and related problems. Adv. Appl. Mech. 30, 259. https://doi.org/10.1016/S0065-2156(08)70176-5, 445.
Kazatchenko, E., Markov, M., Mousatov, A., 2004. Joint modeling of acoustic velocities and electrical conductivity from unified microstructure of rocks. J. Geophys. Res. Solid Earth 109 (B1). https://doi.org/10.1029/2003JB002443.
Kazatchenko, E., Markov, M., Mousatov, A., 2006. Simulation of acoustic velocities, electrical and thermal conductivities using unified pore-structure model of double-porosity carbonate rocks. J. Appl. Geophys. 59 (1), 16–35. https://doi.org/10.1016/j.jappgeo.2005.05.011.
Khazanehdari, J., Sothcott, J., 2003. Variation in dynamic elastic shear modulus of sandstone upon fluid saturation and substitution. Geophysics 68 (2), 472–481. https://doi.org/10.1190/1.1567213.
King, M.S., 1966. Wave velocities in rocks as a function of changes in overburden pressure and pore fluid saturants. Geophysics 31 (1), 50–73. https://doi.org/10.1190/1.1439763.
King, M.S., Marsden, J.R., 2002. Velocity dispersion between ultrasonic and seismic frequencies in brine-saturated reservoir sandstones. Geophysics 67 (1), 254–258. https://doi.org/10.1190/1.1451700.
King, M.S., Marsden, J.R., Dennis, J.W., 2000. Biot dispersion for P-and S-wave velocities in partially and fully saturated sandstones. Geophys. Prospect. 48 (6), 1075–1089. https://doi.org/10.1111/j.1365-2478.2000.00221.x.
Kuster, G.T., Toksöz, M.N., 1974. Velocity and attenuation of seismic waves in two-phase media: Part I. Theoretical formulations. Geophysics 39 (5), 587–606. https://doi.org/10.1190/1.1440450.
Lai, J., Wang, G., Wang, Z., Chen, J., Pang, X., Wang, S., Zhou, Z., He, Z., Fan, X., 2018. A review on pore structure characterization in tight sandstones. Earth Sci. Rev. 177, 436–457. https://doi.org/10.1016/j.earscirev.2017.12.003.
Le Ravalec, M., Guéguen, Y., 1996. High-and low-frequency elastic moduli for a saturated porous/cracked rock-differential self-consistent and poroelastic theories. Geophysics 61 (4), 1080–1094. https://doi.org/10.1190/1.1444029.
Markov, M., Levine, V., Mousatov, A., Kazatchenko, E., 2005. Elastic properties of double-porosity rocks using the differential effective medium model. Geophys. Prospect. 53 (5), 733–754. https://doi.org/10.1111/j.1365-2478.2005.00498.x.
Mori, T., Tanaka, K., 1973. Average stress in matrix and average elastic energy of materials with misfitting inclusions. Acta Metall. 21 (5), 571–574. https://doi.org/10.1016/0001-6160(73)90064-3.
Müller, T.M., Gurevich, B., Lebedev, M., 2010. Seismic wave attenuation and dispersion resulting from wave-induced flow in porous rocks-A review. Geophysics 75 (5), 75A147–75A164. https://doi.org/10.1190/1.3463417.
Norris, A.N., Sheng, P., Callegari, A.J., 1985. Effective-medium theories for two-phase dielectric media. J. Appl. Phys. 57 (6), 1990–1996. https://doi.org/10.1063/1.334384.
O'Connell, R.J., Budiansky, B., 1977. Viscoelastic properties of fluid-saturated cracked solids. J. Geophys. Res. 82 (36), 5719–5735. https://doi.org/10.1029/JB082i036p05719.
Pervukhina, M., Gurevich, B., Dewhurst, D.N., Siggins, A.F., 2010. Applicability of velocity-stress relationships based on the dual porosity concept to isotropic porous rocks. Geophys. J. Int. 181 (3), 1473–1479. https://doi.org/10.1111/j.1365-246X.2010.04535.x.
Pimienta, L., Fortin, J., Guéguen, Y., 2014b. Investigation of elastic weakening in limestone and sandstone samples from moisture adsorption. Geophys. J. Int. 199 (1), 335–347. https://doi.org/10.1093/gji/ggu257.
Pimienta, L., Fortin, J., Guéguen, Y., 2016. Effect of fluids and frequencies on Poisson's ratio of sandstone samples. Geophysics 81 (2), D183–D195. https://doi.org/10.1190/geo2015-0310.1.
Pimienta, L., Sarout, J., Esteban, L., David, C., Clennell, M.B., 2017. Pressure-dependent elastic and transport properties of porous and permeable rocks: microstructural control. J. Geophys. Res. Solid Earth 122 (11), 8952–8968. https://doi.org/10.1002/2017JB014464.
Pimienta, L., Sarout, J., Esteban, L., Piane, C.D., 2014a. Prediction of rocks thermal conductivity from elastic wave velocities, mineralogy and microstructure. Geophys. J. Int. 197 (2), 860–874. https://doi.org/10.1093/gji/ggu034.
Sarout, J., 2012. Impact of pore space topology on permeability, cut-off frequencies and validity of wave propagation theories. Geophys. J. Int. 189 (1), 481–492. https://doi.org/10.1111/j.1365-246X.2011.05329.x.
Sarout, J., Cazes, E., Delle Piane, C., Arena, A., Esteban, L., 2017. Stress-dependent permeability and wave dispersion in tight cracked rocks: experimental validation of simple effective medium models. J. Geophys. Res. Solid Earth 122 (8), 6180–6201. https://doi.org/10.1002/2017JB014147.
Seleznev, N., Habashy, T., Boyd, A., Hizem, M., 2006. Formation properties derived from a multi-frequency dielectric measurement. In: SPWLA 47th Annual Logging Symposium. SPWLA, pp. 1–12.
Shapiro, S.A., 2003. Elastic piezosensitivity of porous and fractured rocks. Geophysics 68 (2), 482–486. https://doi.org/10.1190/1.1567215.
Shafiro, B., Kachanov, M., 1997. Materials with fluid-filled pores of various shapes: effective elastic properties and fluid pressure polarization. Int. J. Solid Struct. 34 (27), 3517–3540. https://doi.org/10.1016/S0020-7683(96)00185-0.
Shapiro, S.A., Khizhniak, G.P., Plotnikov, V.V., Niemann, R., Ilyushin, P.Y., Galkin, S.V., 2015. Permeability dependency on stiff and compliant porosities: a model and some experimental examples. J. Geophys. Eng. 12 (3), 376–385. https://doi.org/10.1088/1742-2132/12/3/376.
Sheng, P., 1991. Consistent modeling of the electrical and elastic properties of sedimentary rocks. Geophysics 56, 1236–1243. https://doi.org/10.1190/1.1443143.
Tang, X., Wang, H., Su, Y., Chen, X., 2021. Inversion for micro-pore structure distribution characteristics using cracked porous medium elastic wave theory. Chin. J. Geophys. 64 (8), 2941–2951. https://doi.org/10.6038/cjg2021O0478.
Tao, G., King, M.S., 1993. Porosity and pore structure from acoustic well logging data. Geophys. Prospect. 41, 435–451. https://doi.org/10.1111/j.1365-2478.1993.tb00578.x.
Toksöz, M.N., Cheng, C.H., Timur, A., 1976. Velocities of seismic waves in porous rocks. Geophysics 41 (4), 621–645. https://doi.org/10.1111/j.1365-2478.1993.tb00578.x.
Tran, D.T., Rai, C.S., Sondergeld, C.H., 2008. Changes in crack aspect-ratio concentration from heat treatment: a comparison between velocity inversion and experimental data. Geophysics 73 (4), E123–E132. https://doi.org/10.1190/1.2928848.
Walsh, J.B., 1965. The effect of cracks on the compressibility of rock. J. Geophys. Res. 70 (2), 381–389. https://doi.org/10.1029/JZ070i002p00381.
Wang, H.M., Tang, X.M., 2021. Inversion of dry and saturated P-and S-wave velocities for the pore-aspect-ratio spectrum using a cracked porous medium elastic wave theory. Geophysics 86 (6), A57–A62. https://doi.org/10.1190/geo2021-0071.1.
Wang, L., Rybacki, E., Bonnelye, A., Bohnhoff, M., Dresen, G., 2021. Experimental investigation on static and dynamic bulk moduli of dry and fluid-saturated porous sandstones. Rock Mech. Rock Eng. 54 (1), 129–148. https://doi.org/10.1007/s00603-020-02248-3.
Wang, X.Q., Schubnel, A., Fortin, J., David, E.C., Guéguen, Y., Ge, H.K., 2012. High Vp/Vs ratio: saturated cracks or anisotropy effects? Geophys. Res. Lett. 39 (11) https://doi.org/10.1029/2012GL051742.
Watanabe, T., Higuchi, A., 2015. Simultaneous measurements of elastic wave velocities and electrical conductivity in a brine-saturated granitic rock under confining pressures and their implication for interpretation of geophysical observations. Prog. Earth Planet. Sci. 2 (1), 1–12. https://doi.org/10.1186/s40645-015-0067-0.
Watanabe, T., Makimura, M., Kaiwa, Y., Desbois, G., Yoshida, K., Michibayashi, K., 2019. Elastic wave velocity and electrical conductivity in a brine-saturated rock and microstructure of pores. Earth Planets Space 71 (1), 1–12. https://doi.org/10.1186/s40623-019-1112-9.
Wu, T.T., 1966. The effect of inclusion shape on the elastic moduli of a two-phase material. Int. J. Solid Struct. 2 (1), 1–8. https://doi.org/10.1016/0020-7683(66)90002-3.
Yamanaka, H., 2001. Application of simulated annealing to inversion of surface wave phase velocity-Comparison of performances between SA and GA inversions. Butsuri-Tansa 54, 197–206.
Yan, F., Han, D.H., Yao, Q., Zhao, L., 2014. Prediction of seismic wave dispersion and attenuation from ultrasonic velocity measurements. Geophysics 79 (5). https://doi.org/10.1190/geo2013-0416.1. WB1-WB8.
Yin, H., Borgomano, J.V., Wang, S., Tiennot, M., Fortin, J., Guéguen, Y., 2019. Fluid substitution and shear weakening in clay-bearing sandstone at seismic frequencies. J. Geophys. Res. Solid Earth 124 (2), 1254–1272. https://doi.org/10.1029/2018JB016241.
Yin, H., Zhao, J., Tang, G., Zhao, L., Ma, X., Wang, S., 2017. Pressure and fluid effect on frequency-dependent elastic moduli in fully saturated tight sandstone. J. Geophys. Res. Solid Earth 122 (11), 8925–8942. https://doi.org/10.1002/2017JB014244.
Zhang, L., Ba, J., Carcione, J.M., 2020. A rock-physics model to determine the pore microstructure of cracked porous rocks. Geophys. J. Int. 223 (1), 622–631. https://doi.org/10.1093/gji/ggaa327.
Zhang, L., Ba, J., Carcione, J.M., Sun, W., 2019b. Modeling wave propagation in cracked porous media with penny-shaped inclusions. Geophysics 84 (4), WA141–WA151. https://doi.org/10.1190/geo2018-0487.1.
Zhang, L., Ba, J., Fu, L., Carcione, J.M., Cao, C., 2019a. Estimation of pore microstructure by using the static and dynamic moduli. Int. J. Rock Mech. Min. Sci. 113, 24–30. https://doi.org/10.1016/j.ijrmms.2018.11.005.
Zheng, J., Zheng, L., Liu, H.H., Ju, Y., 2015. Relationships between permeability, porosity and effective stress for low-permeability sedimentary rock. Int. J. Rock Mech. Min. Sci. 78, 304–318. https://doi.org/10.1016/j.ijrmms.2015.04.025.
Zimmerman, R.W., 1991. Compressibility of Sandstones. Elsevier, Amsterdam.